

The “Triple Point” on 24 May 2002 during IHOP. Part I: Airborne Doppler and
LASE Analyses of the Frontal Boundaries and Convection Initiation

Roger M. Wakimoto, Hanne V. Murphey

Department of Atmospheric Sciences

UCLA

Los Angeles, CA 90095-1565

and

Edward V. Browell, Syed Ismail

NASA Langley Research Center

Hampton, VA 23681-0001

July 15, 2004

Correspond author address: Roger M. Wakimoto, e-mail: roger@atmos.ucla.edu

ABSTRACT

An analysis of the initiation of deep convection near the triple point between a cold front and dryline is presented. High-spatial resolution Doppler wind syntheses combined with vertical cross sections of mixing ratio (q) and aerosol scattering ratio retrieved from a lidar flying over the triple point provide an unprecedented view of the initiation process. The Doppler wind synthesis revealed variability along the dryline similar to the precipitation core/gap structure documented for oceanic cold fronts. Vertical cross sections through the dryline suggest a density current-like structure with the hot and dry air being forced up and over the moist air. Double thin lines associated with moisture gradients were also resolved. The vertical profile of retrieved q , approximately perpendicular to the dryline, showed a pronounced jump in the depth of the moisture layer across the triple point. Analyses of dropsonde data show the existence of virtual potential temperature (θ_v) gradients across the cold front and the dryline. Although the vertical velocity was strong at the triple point, deep convection initiated ~ 50 km to the east. The location where convection first developed was characterized by a prominent aerosol and moisture plume, reduced static stability, and the largest potential instability. An internal gravity wave may have provided the lift to initiate convection.

1. Introduction

In recent years, the initiation of convection has garnered increasing interest. In particular, summertime convection that develops under weakly-forced synoptic flow has remained a challenging research and operational problem. Surface convergence zones or boundaries are known to play an important role in convection initiation under these synoptic conditions. Purdom (1982) was among the first to quantify the dominant role that intersection and merger of boundaries play in the initiation of convection. Wilson and Schreiber (1986) suggest that 55% of boundaries that intersect (i.e., cases where the boundaries intersect at an angle $>30^\circ$) produce new storms. The point of intersection is often referred to as a “triple point” where three distinct air masses converge (e.g., Reed and Albright 1997, Weiss and Bluestein 2002).

There have been a number of cases presented in the literature focusing on convection developing near the intersection between a front (or baroclinic boundary) and the dryline (e.g., Bluestein and Parks 1983, Schaefer 1986, Bluestein et al. 1990, Hane et al. 1993, Parsons et al. 1991, 2000, Neiman and Wakimoto 1999, Weiss and Bluestein 2002). The dryline separates moist air from the Gulf of Mexico from dry air flowing off the semi-arid high plateau regions of Mexico and the southwest (Rhea 1966, Schaefer 1974, 1986)¹. Few of these past studies, however, have provided detailed measurements documenting this process. Moreover, only the study by Weiss and Bluestein (2002) present high-resolution analyses of the triple point.

¹ The dryline’s association with severe convection has been well established (e.g., Rhea 1966, Bluestein and Parker 1993).

A strong cold front moved southward through Oklahoma and the Texas Panhandle on 24 May 2002 during IHOP (International H₂O Project). The front intersected the dryline in the Panhandle producing a well-defined triple point. Several research aircraft and mobile ground teams converged near Shamrock, Texas while collecting detailed observations of the dryline, cold front, and the triple point. Deep convection subsequently initiated near the triple point. This case is unique since it combines airborne Doppler radar syntheses, in-situ flight level data, dropsondes, and water vapor/aerosol measurements from an airborne lidar into a comprehensive analysis of this event. This is the first of a series of papers documenting the meteorological events on this day. Other studies will include an analysis of the multi-Doppler synthesis from several ground-based radars of the triple point with high temporal resolution (C. Ziegler, personal communication 2004), and the finescale vertical structure of the cold front and dryline using an airborne cloud radar. Section 2 briefly describes IHOP and the data methodology. The environmental conditions and aircraft flight tracks are presented in section 3. ELDORA and LASE analyses are shown in sections 4 and 5, respectively. A summary and discussion are presented in section 6.

2. IHOP and the data methodology

IHOP was a large multiagency international field campaign operated from 13 May to 25 June 2002 over the southern Great Plains (Weckwerth et al., 2004). The principle objective of IHOP was to obtain an improved characterization of the time-varying three-dimensional water vapor field and to evaluate its utility in improving the understanding and prediction of convective processes.

One of the main research components of IHOP was to further the understanding and eventually the prediction of processes that determine where and when convection forms. The experiment utilized a plethora of mobile ground-based and airborne instruments. The following discussion highlights the main instruments used in this study.

a. ELDORA

ELDORA (Electra Doppler Radar) is a Doppler radar platform onboard an NRL (Naval Research Laboratory) P-3 that collects detailed observations in the along-track direction by using a fast rotation rate of the antenna. Increased sensitivity of ELDORA was achieved by the selection of a longer pulse length (i.e., transmits more power). The latter characteristic is critical for the current study since it allows ELDORA to detect echoes and Doppler velocities within the clear air (see Wakimoto et al. 1996 for select examples). In particular, the P-3 mission was to fly at low levels (~400 m above ground level (AGL); hereafter, all heights are AGL except where indicated) and parallel to the radar-detected thin lines (e.g., Wilson and Schreiber 1986) associated with boundaries. The thin line was located 2-3 km from the aircraft if the pattern was executed correctly. The track enclosed the thin line in a box-shaped pattern with the legs 75-80 km long and parallel to the line. This flight pattern was difficult to execute and required continuous corrections to the aircraft heading by the mission scientist owing to the non-linear nature of many of the boundaries. Raw ELDORA scans which revealed the location of the thin line in real time were used to adjust the flight track. The capabilities of ELDORA are discussed in detail by Hildebrand et al. (1994, 1996)

and Wakimoto et al. (1996) and the list of scanning parameters implemented during data collection on this day is shown in Table 1. The interested reader is referred to Hildebrand et al. (1994, 1996) for a comprehensive discussion of the radar design of ELDORA.

ELDORA uses a multiple beam technique referred to as fore-aft scanning or FAST. This technique requires the antennae onboard the aircraft to be scanning fore and aft relative to the normal to the fuselage by $\pm 18.5^\circ$. Accordingly, the angle of intersection of the radar scans is nominally 37° . This angle was chosen to minimize the time between points where the fore and aft scans intersect while ensuring that the geometric angle of intersection between the beams is large enough to lower the standard deviations of the estimates of the three-dimensional wind field to an acceptable level. A complete description of this scanning methodology can be found in Jorgensen et al. (1996). A discussion of the Doppler radar wind synthesis is presented in the appendix.

The advantage of the P-3 flight track was the ability to resolve the kinematic variability of the convergence boundaries in the along-line direction over an extended path. This has rarely been accomplished in past field programs. The work described by Atkins et al. (1998) is one notable exception. The main disadvantage in the flight track was the time required to execute one leg (~ 12 min), which decreases the temporal resolution. The IHOP scientists felt that the advantage of this flight pattern far outweighed the disadvantage. Moreover, the ground-based mobile Doppler radars deployed during IHOP, positioned approximately in the center of the P-3 analysis areas, would collect the high temporal data albeit in a smaller domain. It is the latter analysis that is presented in a companion paper.

Leandre II is an airborne water vapor DIAL (differential absorption lidar) built by CNRS (Centre National de la Recherche Scientifique) in France. The lidar was installed onboard the P-3 in a horizontally-pointing mode during the convection initiation missions. The plan was to combine the clear-air dual-Doppler wind syntheses from ELDORA with a horizontal mapping of the water vapor field. The airborne mission on 24 May was one of the first to deploy Leandre II. Unfortunately, the lidar was not set at the proper horizontal viewing angle and no usable data were collected on this day.

b. LASE

LASE is another water vapor DIAL system that was operated by the NASA (National Space and Aeronautic Administration) Langley Research Center during IHOP. It was placed on a DC-8 in a vertically downward-pointing mode during the experiment (Browell et al. 2003). The transmitter consists of a Ti:sapphire laser pumped by a double-pulsed Nd:YAG laser. The frequency of the Ti:sapphire laser is controlled by injection seeding using a diode laser that is frequency locked to a water vapor line in the 815-nm region. The “on” and “off” DIAL wavelengths are separated by less than 70 pm (10^{-12} m), and the laser pulses are sequentially transmitted with about 400 μ s separation. The LASE (Lidar Atmospheric Sensing Experiment) system has proven to be a reliable, accurate, and sensitive water vapor profiler with the ability to measure water vapor mixing ratios over a large dynamic range (0.01 to 20 g kg⁻¹) (see Browell et al. 1997). During IHOP, the LASE water

vapor measurements had a vertical resolution of 330 m and a horizontal resolution of about 14 km (Browell et al. 2003). Aerosol backscatter ratios [defined as the ratio of the aerosol and molecular (or total) backscatter coefficient to the molecular backscatter coefficient] can be simultaneously measured with a vertical resolution of 30 m and a horizontal resolution of 40 m. The DC-8 flew at ~7 km over the region of interest on this day.

3. Environmental conditions and the aircraft flight tracks

A prominent short-wave trough was apparent at the 500-mb level over western Colorado and New Mexico (not shown) at 1200 UTC 24 May (hereafter, all times are UTC. UTC = LT + 5 h). Strong winds (greater than 25 ms^{-1}) at the 850-mb level were advecting moisture from the Gulf of Mexico into Oklahoma and eastern Texas in advance of this upper-level trough (not shown). The 500-mb trough moved rapidly to the east and was located over the Texas Panhandle by 0000. A well-defined surface frontal zone, oriented northeast to southwest extended from the northeastern United States into the Texas Panhandle. The orientation of the front changed to approximately east-west in the Panhandle (Fig. 1). The positions of the thin lines as observed by the WSR-88D radars located throughout the IHOP domain, and in situ measurements by the P-3 were used to accurately locate fronts and the dryline between the surface stations.

The positions of the cold front and dryline are apparent in the surface analysis at 1900 (Fig. 1a). Stratus clouds can be seen to the north of the front within the relatively cold, northerly flow. Cumulus clouds are located throughout the tropical air mass to the east of the dryline while the

skies are clear to the west of dryline where the air is hot and dry. A secondary boundary exists, east of the dryline and along the Texas/Oklahoma border and is apparent in the converging winds and small dew-point discontinuity. IHOP forecasters believed that this boundary was a remnant outflow boundary from convection that had developed the previous night.

The P-3 entered the Texas Panhandle at ~1900 and initiated its first flight leg at 1915. The aircraft flew its primary legs along the dryline and endeavored to fly into the cold front as close as possible to the triple point (Fig. 1a). The cold front continued to move to the southeast at 2000, and convection began to initiate near the dryline (Fig. 1b). The convection first developed to the south with new cells forming further to the north. Interestingly, the convection developed *along* the dryline to the south but *east* of the dryline closer to the triple point. The convection continued to intensify and organized into a squall line associated with prominent cirrus anvils at 2100 (Fig. 1c). Most of the region east of the dryline is covered with cirrus anvils at 2200, and the post-cold frontal winds appear to have increased in speed (Fig. 1d). Although convection initiating along the dryline is common, it can frequently develop east of the line (e.g., Rhea 1966, Ogura et al. 1982, Schaefer 1986)². The P-3 continued to collect data on the dryline, cold front and triple point until 2049. Also shown in Fig. 1b is the west-east flight leg by the DC-8 near the triple point.

Surface analyses at the same four times shown in Fig. 1 are superimposed onto WSR-88D

² It is also possible that clouds that initiate along the dryline can be advected eastward before hydrometeors can form to radar detectable size. This can give the appearance of initiation east of the dryline (Hane et al. 2001).

surveillance scans from Amarillo, TX in Fig. 2. Unfortunately, the triple point was ~100 km from the radar location. Accordingly, the radar thin lines are apparent in the clear air return but not resolved with high spatial resolution. The P-3 flight tracks paralleling the thin line associated with the dryline are indicated (Figs. 2a, b, and c) as well as the DC-8 track flown near the triple point (Fig. 2b). The subsequent squall line was intense with maximum echo intensities greater than 60 dBZe for several of the embedded cells (Figs. 2c and d). Also shown in Fig. 2b are the deployment points along a west-east line for a series of dropsondes from a Learjet between 2022 - 2046. The dropsondes documented the kinematic and thermodynamic structure of both the cold front and the dryline.

4. ELDORA analyses

a. 1915 – 1926 UTC

The ELDORA Doppler wind syntheses at 600 m for the first pass along the dryline from 1915 – 1926 is shown in Fig. 3. The aircraft flew west of and parallel to the dryline during this pass. The thin lines associated with the cold front and dryline are evident (Fig. 3a). Winds were westerly within the hot, dry air west of the dryline and southwesterly in the warm, moist air east of the dryline (Fig. 3). The intersection of these two lines at the triple point is also apparent. An enlargement of the region surrounding the triple point is shown in Fig. 4a. The radar echoes along the thin line associated with the cold front were stronger than the dryline in this and subsequent

analyses. In addition, the strongest echoes along the thin line occurred near the triple point (Figs. 3 and 4a). This suggests that horizontal convergence was strongest in this region (e.g., Wilson et al. 1994). This was confirmed by the derived convergence fields (not shown) and the maximum vertical velocities $> 2 \text{ ms}^{-1}$ (Figs. 3b and 4a). The updrafts along the cold front, in general, were stronger than along the dryline.

Although not readily apparent in the surface analyses shown in Figs. 1 and 2, a cyclonic mesoscale circulation was centered near the triple point shown in Figs. 3 and 4a. The vertical vorticity within the circulation is $> 2 \times 10^{-3} \text{ s}^{-1}$. The ridges of the vertical vorticity isopleths extended along the cold front in response to the strong cyclonic shift at the frontal boundary. Cyclonic circulations at the apex of the dry and hot wedge of air near the triple point have been documented before (Parsons et al. 2000) but have not been previously resolved with the detail shown in Fig. 3.

The dryline thin line is characterized by cellular structure (Fig. 3a) reminiscent of the precipitation core/gap structure documented along oceanic cold fronts (Hobbs and Biswas 1979, James and Browning 1979). Variability in the echo pattern along the dryline was also shown by Atkins et al. (1998) and attributed to horizontal convective rolls (HCRs) intersecting the boundary. HCRs frequently develop in the atmospheric boundary layer and consist of pairs of counterrotating helices with their major axis oriented near parallel with the mean wind and are one of the most common forms of boundary layer convection (e.g., Kuettner 1959, Asai 1970, LeMone 1973, Brown 1980, Weckwerth et al. 1997).

In situ data collected by the P-3 during this pass reveal the thermodynamic and kinematic

structure of the cold front and dryline at flight level (Fig. 5). The plot shown in Fig. 5a includes the time when the aircraft penetrated the dryline at ~1923 and briefly sampled the moist air before it passed through the cold front. There was a distinct rise in equivalent potential temperature (θ_E) and mixing ratio (q) across the dryline. The penetration of the dryline is surprising since the flight track was essentially a straight line (Figs. 3 and 4a) and suggests that there was a change in the orientation of the dryline near the triple point. No obvious discontinuity in virtual potential temperature (θ_v) could be identified. There was a small cyclonic shift in the winds across the dryline and the wind speeds decreased.

There was a rapid drop in θ_v when the P-3 penetrated the cold front at ~1923:45 (Fig. 5a) followed by a slower decrease further to the north. The equivalent potential temperature during the same time interval fluctuated before falling at ~1924:20. The post-frontal winds increased in speed and shifted to a more northerly direction.

The dryline was sampled at another location during an east to west penetration, approximately 100 km to the south of the triple point (Fig. 5b). The characteristic drops in θ_E , q , and a wind shift are apparent as the aircraft flew through the dryline into the semi-arid air. There is also a suggestion that θ_v was greater on the moist side of the dryline. There has been an ongoing debate in the literature concerning the existence of a gradient of θ_v across the dryline (Ziegler and Hane 1993, Doswell and Bosart 2001). Schaefer (1986) and Crawford and Bluestein (1997) propose the virtual potential temperature gradient across the dryline is nonexistent or negligibly small. On the other hand, Parsons et al. (1991), Ziegler and Hane (1993), Hane et al. (1997), and Atkins et

al. (1998) have shown the existence of a horizontal gradient of θ_v of about 1 K over 8 km with lower values on the moist side. The flight-level data suggests little or no density contrast across the dryline existed on this day. Dropsonde data to be presented in section 5, however, do reveal the existence of a gradient of θ_v .

The vertical structure of the dryline is revealed in the raw scans collected by ELDORA. The dryline thin line is ~ 2 km deep with maximum radar reflectivities of ~ 10 dBZe (Fig. 6). The single Doppler velocities suggest low-level convergence and upper-level divergence at the dryline boundary as shown by the black arrows. In addition, the hot and dry air located west of the dryline appears to flow up and over the moist air in Fig. 6 similar to the lidar observations presented by Parsons et al. (1991). There also appears to be descent of the flow 3-4 km east of the dryline. Such descent has been proposed by Hane et al. (1993) to be the downward branch of the dryline solenoidally-driven circulation owing to a gradient in θ_v across the dryline (the existence of the θ_v - gradient will be shown in section 5).

The mean kinematic structure of the dryline was examined by averaging 80 vertical cross sections perpendicular to the dryline (Fig. 7) over a distance of 48 km (i.e., 80 grid points separated by 600 m). Great care was taken to select those cross sections in which the airflow was not influenced by the approaching cold front. The hot and dry air is being forced over the moist air at the location of the thin line (Fig. 7a), consistent with the single-Doppler image (Fig. 6). There is weak descent to the west of the dryline and a suggestion of downflow ~ 5 km to the east of the thin line. The latter was also suggested in the velocity image shown in Fig. 6. The general features

shown in Fig. 7a are similar to those proposed by Ziegler and Hane (1993, see their Fig. 14) based on aircraft measurements.

An interesting feature is the westward tilt with increasing height of cyclonic vertical vorticity (Fig. 7b). In addition, there is a negative vorticity above the thin line. The vorticity structure shown in the figure is counterintuitive if the dryline behaves like a density current as suggested by Parsons et al. (1991), Ziegler and Hane (1993), and Ziegler et al. (1995). The maximum in positive vorticity would typically slope over the denser air mass (i.e., to the east in the present case).

There is weak convergence in the component of flow in the plane of the cross section at the location of the thin line (Fig. 7c). The strongest vertical wind shear exists over and to the east of the dryline with the strongest westerly flow aloft located slightly to the east of the thin line (also noted by Hane et al. 1993 and Ziegler and Hane 1993). This structure would be expected if a solenoidally-driven circulation were superimposed on the ambient flow.

b. 1931 – 1942 UTC

The P-3 reversed its heading and flew back through the cold front and the mesoscale circulation between 1931 – 1942 (Figs. 4b and 8). The thin line associated with the cold front assumed a slight “S-shape” pattern in response to the southerly and northerly flow east and west of the circulation center, respectively. The isopleths of positive vertical velocity and vorticity are elongated along the cold front, similar to the results shown in Fig. 3. Their peak values at the triple point have increased to $>3 \text{ m s}^{-1}$ and $3 \times 10^{-3} \text{ s}^{-1}$, respectively. The plot in Fig. 4b reveals that the P-3

flew directly through the maximum in vertical vorticity and the triple point. The primary goal of this southerly track was to fly parallel to the dryline but on the moist side of the boundary. The aircraft, however, initially straddled the dryline (see Figs. 4b and 8) before crossing over to the moist side at ~1938.

Another thin line of radar reflectivity can be identified in Fig. 8. It is located ~10 km to the east of the dryline echo pattern. Multiple thin lines in the vicinity of drylines have been previously documented. They often are associated with surface convergence and moisture gradients (e.g., Hane et al. 1993, 2001, 2002). These secondary lines may also play an important role in the discreet eastward propagation of the dryline although the mechanisms that produce these multiple lines are not clearly understood. The mixing ratio recorded at flight level fluctuated between moist and dry conditions between 1934:00 – 1937:30 when the aircraft straddled the thin line (not shown). There was an ~1.5 g kg⁻¹ increase in q at ~1942:30 (not shown) when the P-3 penetrated the eastern thin line (see the bottom of Fig. 8). These observations suggest that the eastern thin line was also a moisture discontinuity as discussed by Hane et al. 2001, 2002). Another example of a secondary thin line is presented in more detail in section 4d.

It should be noted that the absence of this eastern thin line during the previous pass (Fig. 3) is most likely owing to its location. The typical maximum range that ELDORA was able to detect clear air return on this day was ~10 km. Accordingly, the eastern thin line may have been present during the pass depicted in Fig. 3, however, it was located at a range that exceeded the radar's ability to detect it.

c. 1949 – 1959 UTC

The third flight leg was similar to the first with the P-3 flying parallel to and on the western side of the dryline (Fig. 9). ELDORA was able to detect a larger fraction of the cold front during this pass. The nonlinear nature of the frontal boundary is readily apparent and the dry, hot air between the front and the dryline is now a narrow corridor that is 15-20 km wide. The triple point moves to the south as the front moves to the southeast in a process that resembles the closing of a “zipper”. The mesoscale circulation does not follow the triple point but appears to be displaced to the northeast. As a result, the post-frontal winds are primarily from the north in Fig. 4c.

One of the best views of the merger of the cold front and dryline is presented in a series of raw ELDORA scans collected by the P-3 (Fig. 10). The sequence of images shown in the figure began soon after the P-3 passed through the cold front. Fortunately, the viewing angle of the radar is nearly perpendicular to both the cold front and the dryline (Fig. 9). Although the images were collected at different locations along the front, they can also be viewed as an approximate time evolution of the merger process under some restrictive assumptions (e.g., no along-frontal variation for either boundary). Other scans recorded by ELDORA support the scenario depicted in Fig. 10.

The echoes that comprise the cold front thin line are more intense than the dryline in all of the scans. There is markedly post-cold frontal air at low levels in all of the Doppler scans as the cold front moves to the south. The images infer a plume of hot, dry air mass being deflected over the moist air as indicated by the black arrow. The velocity pattern shown in the scan at 1957:53

(Fig. 10c) suggests that this deflected flow covers a more extensive area as the thin lines merge. Also evident in Fig. 10b are several rotational couplets along the cold frontal interface indicating the presence of KH billows. Such circulations have been documented before atop the post-frontal flow as shown by Young and Johnson (1984) and Shapiro et al. (1985).

The three-dimensional kinematic wind field synthesized from the ELDORA data provides another view of the merger process. Two vertical cross sections depicting the front/boundary locations are shown in Fig. 11. The boundaries were kinematically determined by noting discontinuities in the wind field. The portion of the dryline that is dashed in cross section B-B' is an estimated position.

The cold front is ~ 4 km northwest of the dryline in cross section A-A' (Fig. 4c). The maximum updrafts at the leading edge of the front are $\sim 3 \text{ m s}^{-1}$ (Fig. 11). The updrafts near the dryline are weaker as flow moves up and over the moist air. The thin lines have merged in cross section B-B' although two distinct reflectivity maxima associated with the cold front and dryline can still be identified. The updrafts in the merged region are stronger suggesting that moist air is being lifted to higher altitudes. The backing of winds with increasing height through the cold front is apparent and indicates that the northerly flow was only 1 km deep. This pattern also suggests that the frontal surface was not steeply inclined near its surface position.

d. 2004 – 2014 UTC

By 2000, storms were developing to the east of the dryline. Several echoes are apparent

in the WSR-88D images from Amarillo (~150 km along the 120° azimuth in Fig. 2b). The anvils of these small storms also appear in Fig. 1b at the northern end of the line of towering cumulus. The P-3 sampled the dryline and cold front from 2004:04 – 2114:30 north and west of where these echoes were developing. The wind syntheses shown in Figs. 4d and 12 reveal stronger northerly flow behind the cold front compared with the earlier analyses. Of particular interest is the double thin line structure located ~20 km south of the triple point (Fig. 12) and is similar to that noted in Fig. 8. This section of the dryline is enlarged in Fig. 13.

As previously mentioned, multiple thin lines near the position of the dryline have been noted before. Hane et al. (2002), based upon in situ measurements, found that these thin lines in a synoptically-active environment are often associated with wind and moisture discontinuities. The more distinct thin lines are associated with stronger horizontal convergence across the line. They may also be related to the discontinuous movement of the dryline. Indeed, Hane et al. (2001) suggest that an eastward redevelopment of the dryline was characterized by a series of ‘steps’ in the boundary layer moisture pattern. The westernmost and easternmost steps coincided with the locations of the dryline before and after redevelopment, respectively. Other possible explanations for multiple moisture gradients include compensating downdrafts east of the main dryline (Hane et al. 1993, Ziegler and Hane 1993, Ziegler et al. 1995, Shaw et al. 1997) or HCRs forming in the convective boundary layer (Atkins et al. 1998, Hane et al. 2001).

There is one thin line denoting the dryline apparent in the southern section of the analysis shown in Fig. 13 (also seen in Fig. 12). There is a prominent windshift from westerly to south-

westerly flow across this boundary. The gradient of isogons is different in the region where the double thin lines exist. There is a partial windshift across the western thin line and an even smaller shift in wind direction across the eastern line. Fortunately, the track flown by the P-3 was ideal for sampling the multiple air masses present on this day.

The aircraft initially flew within the air mass north of the cold front as shown in the time series presented in Fig. 14 (see Fig. 13 for location). This cool air is also moist and accompanied by brisk winds from a northerly direction. The P-3 penetrated the cold front at the triple point and emerges on the west side of the dryline (note that the aircraft position is west of the dryline thin line and q is less than 7 g kg^{-1} after ~ 2007 in Figs. 13 and 14, respectively). Subsequently, the aircraft drifted to the moist side of the dryline as shown by the rising mixing ratio values and the cyclonic turning of the winds from 2007 - 2009. From 2009:10 – 2011:40, the P-3 is positioned between the two thin lines where q is nearly constant at $\sim 9 \text{ g kg}^{-1}$. The aircraft penetrated the location where the two thin lines merge and emerged on the eastern edge of the main thin line after $\sim 2011:40$. Note that after the penetration of the merger point, q and θ_E rise to $\sim 10 \text{ g kg}^{-1}$ and $\sim 338 \text{ K}$, respectively, and the wind direction shifts to a more southerly direction. The virtual potential temperature remains steady. These observed discontinuities through secondary thin lines are consistent with those reported by Hane et al. (2001). In addition, the observed thin line structure shown in Fig. 12 is similar to the distribution of moisture gradients determined from aircraft data collected at flight level by Hane et al. (1997, 2002). They suggest that both single and multiple moisture gradients could exist concurrently along the same dryline.

e. 2024 – 2034 and 2038 - 2049 UTC

The last two passes by the triple point were executed from 2024 – 2034 and 2038 – 2049 (Fig. 15). Deep convection continued to initiate and by 2100 a squall line is apparent in Figs. 1c and 2c. ELDORA detected these intense echoes at a range of ~50 km to the east of the dryline (not shown). The triple point was distinct and formed a “T-intersection” during early passes by the P-3 (e.g., see Fig. 3). However, the triple point is more difficult to identify in Fig. 15a but is located near 2032 along the flight track. The triple point during the next pass (Fig. 15b) is not readily apparent as the cold front continues to move southeast and merge with the dry line. Indeed, even the dryline is difficult to locate at the latter time. The flight level data from 2044 – 2049 (not shown) revealed mixing ratios fluctuating between 8 and 10 g kg⁻¹; i.e., between the values that were characteristic of the dry and moist air masses, respectively. This suggests that the convective boundary layer was turbulent and substantial mixing between air masses was occurring. Accordingly, the precise position of the dryline is difficult to determine at this time.

The thin line located ~10 km to the east of the flight track in Fig. 15b may be a secondary thin line. Unfortunately, the aircraft did not fly through the line so thermodynamic data on the eastern side of this line were unavailable. The P-3 terminated radar data collection after 2049. This decision was made by the mission scientist onboard the aircraft since the deep convection located to the east of the cold front/dryline resulted in severe second-trip echo contamination from intense storms beyond the unambiguous range of the radar (see Doviak and Zrníc 1993). Accordingly,

subsequent flight legs would not have collected usable Doppler velocity data.

5. LASE and dropsonde analyses

One of the critical aspects of the current study was the fact that convection did not initiate at the triple point even though the updrafts were enhanced in this region by the merger of the cold front and the dryline (see Fig. 11). Instead, the convection formed ~50 km to the east of the dryline/triple point. This is not unusual, however. Rhea (1966) was among the first to document this eastward bias, especially for lines of storms. The reasons for the displacement between the initiation of convection and the dryline are not well understood. This section examines the vertical structure across the dryline and cold front using a combination of the measurements from the LASE lidar on board the DC-8 and a series of dropsondes deployed by a Learjet.

The DC-8 departed from Oklahoma City at 1730. Its mission was to fly west-east legs ~400 km long to map out the vertical structure of the moisture pattern centered over the Texas Panhandle and western Oklahoma. A total of 8 legs were flown over the region. The most important pass by the aircraft was 1950 – 2021 when the following objectives were met:

1. The DC-8 flew directly over the box pattern flown by the P-3.
2. The DC-8 track flew in coordination with the Learjet while the latter deployed a series of dropsondes.
3. The west-east leg by the DC-8 was flown ~30 min before deep convection initiated in the region.

The flight track of the DC-8 superimposed onto a satellite image at 2000 is shown in Fig. 1b. The DC-8 leg was well-positioned as it flew near the center of the elongated box pattern flown by the P-3. As previously mentioned, deep convection was initiating to the south but would soon form an intense squall line near the eastern border of the Texas Panhandle into Oklahoma (Figs. 1c and d).

The flight track of the DC-8 is superimposed onto the WSR-88D scan in Fig. 2b. The position of the thin lines in the figure reveal that the DC-8 flew near the triple point. This is confirmed by the syntheses shown in Figs. 4d and 12 suggesting that the aircraft flew directly over the intersection of the dryline with the cold front. The coordination of the DC-8 and P-3 was excellent since the difference in time at the crossing point of the two aircraft tracks at the triple point was only 3 minutes (Fig. 4d). A sequence of dropsondes were released from 2022 – 2046 from a Learjet. The release points of the dropsondes were south of the triple point (shown by the open circles in Fig. 2b).

Past analyses of the vertical structure of the dryline were based on in situ measurements by an aircraft flying a stepped traverse pattern (e.g., Ziegler and Hane 1993, Hane et al. 1997, and Ziegler and Rasmussen 1998). As a result, the data collection was typically limited to low altitudes and the dryline was assumed to be steady for times that often exceeded 70 min. In the present study, the dropsondes were deployed in ~20 min over a distance that covered >200 km (average horizontal spacing of the dropsondes was ~30 km). In addition, the dropsondes were deployed from a height of ~5.0 km mean sea level (MSL).

The dropsonde and LASE data provided a unique opportunity to integrate the data sets into

a single vertical cross section since the coordination between the DC-8 and Learjet was very good. There was a 17–24 min difference between the longitudinal positions of the two aircraft along the west-east track and they were also separated by ~25 km in the north-south direction. In combining the dropsonde and lidar data collected by LASE, it is assumed that there was little change of the thermodynamic and kinematic structure in the north-south direction. It is possible that variations owing to the core/gap structure along the dryline may impact the interpretation of the results.

The merged data set is presented in Fig. 16. The vertical wind profile depicts the northerly flow behind the cold front, the southeasterly flow to the east of the dryline, and the southwesterly flow aloft. The vertical structure of q retrieved by LASE is shown in Fig. 16a. The white areas represents blockage of the lidar beam by intervening clouds. The main attenuation is caused by the low-level stratus clouds located well to the rear of the cold front and the cumulus clouds developing along and east of the dryline. Both cloud types can be identified in the satellite image (Fig. 1b).

There is excellent agreement between the isopleth analysis of q based on the dropsonde data and the moisture fields derived from LASE. The striking feature depicted in Fig. 16a is the increase in the depth of the moist layer from west to east across the triple point, e.g., the 6 g kg^{-1} isopleth experiences a greater than 1 km increase in height across the region. There is also an upward bulge in q at 2013 - 2014 along the DC-8 flight track (note the 2 g kg^{-1} isopleth). Two pockets with maximum q values ($>13 \text{ g kg}^{-1}$) exist at low levels and east of the dryline. The eastern maximum may be the result of a second dryline located 50-60 km east of the triple point (e.g., Hane et al. 2001, Crawford and Bluestein 1997, Ziegler and Rasmussen 1998).

The orientation of the q contours in Fig. 16a suggests that the cold dense air behind the cold front is undercutting the moist air east of the dryline. This interpretation is consistent with the θ_v profile (Fig. 16b). The θ_v analysis in the figure is superimposed onto a plot of the aerosol scattering ratio from LASE. Although the in situ penetrations by the P-3 suggested no discontinuity in θ_v across the dryline (Figs. 5b and 14), the results presented in Fig. 16b reveal that a θ_v -gradient did exist with cooler air located to the east of the dryline within the moist air. The lack of a gradient in the in situ measurements presented earlier is likely the result of the relatively short distance of the flight legs across the dryline. Apparently, the θ_v -gradient at the dryline was relatively weak and difficult to measure over these distances. In contrast, the dropsonde and lidar data cover a distance that is nearly an order of magnitude greater. The combined solenoidally-driven circulations by the cold front and the dryline would produce significant updrafts near the triple point (shown in Fig. 11). The circulation produced by solenoid effects would also explain the similar kinematic structure of the dryline with a density current as observed in the ELDORA data.

The depth of the convective boundary layer (CBL) east of the dryline is 2.5 - 3 km MSL and is apparent as the enhanced return in the aerosol scattering ratio (note the darker red colors). The gray areas in the figure represent significantly enhanced scattering from clouds. Note the upward slope of the stratus clouds to the west behind the surface position of the cold front, which is related to the frontal slope. The distribution of aerosols clearly reveals two rising plumes. The plumes are located above the triple point (highlighted by the single black arrow) and ~50 km east of the merger (indicated by the two black arrows). The latter plume is important since this is the location

where deep convection first initiates (the position of the eastern plume relative to the triple point is indicated by the "X" in Figs. 1b and 2b). This rising plume diverges between 4-5 km MSL producing an anvil-like structure. Not surprisingly, this eastern aerosol plume is also the position where the upward bulge in mixing ratio was noted (Fig. 16a). Accordingly, the LASE data reaffirms that deep convection did not form at the triple point even though there was vigorous lifting indicated by the aerosol plume and the dual-Doppler wind syntheses (Fig. 11).

Close examination of the θ_v analysis suggests that the eastern aerosol plume is located in a region where the stability is reduced (i.e., $\partial\theta_v/\partial z$ is reduced) between 3 - 4 km MSL. This reduction is produced by a 'dip' in the 310 K isopleth just west of the plume. This dip is consistent with the top of the CBL, which is also depressed based on the aerosol plot (Fig. 16b). This depression could be a result of forced descent by the dryline solenoidal circulation as hypothesized by Hane et al. (2001). It is also possible that this feature is a result of an internal gravity wave. The wave could have been generated by the collision of the cold front and the dryline (e.g., Simpson 1997). A case study by Koch and McCarthy (1982) suggests that lifting by gravity waves could release potential instability and initiate deep convection near the dryline. Indeed, the largest potential instability, based on the θ_E profile, is collocated with the eastern plume (Fig. 16c). The advection of moisture to higher levels is also evident by the upward displacement of the 321 K isopleth of θ_E . Unfortunately, the dearth of surface stations near the triple point hampered a detailed examination of the pressure traces which might have supported the existence of a gravity wave.

6. Summary and discussion

An analysis of the initiation of deep convection near the intersection of a cold front and dryline (i.e., a triple point) was presented. The airborne Doppler analyses of the dryline revealed variability along the radar-detected thin line that was similar to the precipitation core/gap structure documented along oceanic cold fronts. The vertical structure obtained from Doppler wind syntheses and RHI scans suggests that the dryline exhibited a density current-like structure with the dry, hot air being forced over the moist air. A double thin line structure separated by ~ 8 km was documented. The western thin line was the primary dryline discontinuity, however, the eastern thin line was also accompanied by wind and moisture discontinuities.

The Doppler wind syntheses showed that the largest vertical vorticity and velocity values were confined to the triple point. Vertical cross sections of the retrieved q and aerosol scattering ratio from an airborne lidar were merged with dropsonde data. A pronounced jump in the height of the moist layer was noted across the triple point. Cold pools of air were shown to exist to the west of the cold front and also east of the dryline. The gradient in θ_v across the dryline, however, was weak. The solenoidally-generated circulation was responsible for the density current structure observed by the airborne radar.

The aerosol and q distributions observed by the airborne lidar revealed two plumes of rising air. One was located near the triple point, as expected, while the other was ~ 50 km to the east. Interestingly, deep convection initiated at the location of the eastern plume rather than over the triple point. The eastern aerosol plume developed in an area of reduced static stability and high

potential instability. In addition, there was a suggestion in the aerosol profile and the θ_v analysis that an internal gravity wave was present. It is speculated that the wave may have been produced by the collision of the cold front and the dryline. This wave may have provided additional lift to air parcels in the region.

This is the first in a series of papers documenting this event. Other studies include a detailed kinematic analyses of the triple point based on an array of ground-based mobile radars and high-resolution observations of the cold front and dryline with airborne cloud radar.

Acknowledgement: LASE participation in IHOP was supported by Dr. Jim Dodge of NASA's Office of Earth Sciences. We recognize the significant contributions of Dr. Richard A. Ferrare, Susan Kooi, Carolyn Butler, and Anthony Notari in obtaining and processing the LASE data discussed in this paper. The other research results presented in this paper were supported by the National Science Foundation under Grants ATM-0121048.

Appendix

Doppler Radar Wind Synthesis

The along track and sweep angle resolutions were ~ 550 m and 1.5° , respectively, during IHOP. This sweep angle resolution resulted in an effective sampling in the vertical of ~ 250 m in the analysis domain. As a result, the reflectivity and Doppler velocity data were interpolated onto a Cartesian grid with horizontal and vertical grid spacing of 600 and 300 m, respectively. The lowest grid level was located at 300 m AGL.

The dryline was the primary focus of the analyses and it was essentially stationary during period under investigation. The individual motion caused by the along-line variability was assumed to be small. Accordingly, the individual radar scans for each pass were not time-space adjusted for this study. The cold front, however, was moving at ~ 6.1 m s⁻¹ from 330° . All of the wind syntheses were rerun using the cold front motion to advect the individual radar scans (not shown). These new syntheses were compared with the ones presented in this paper. There were only minor changes in the wind, vertical velocity and vorticity fields along the cold front. These changes would not have altered any of the conclusions presented in the paper. The negligible effect is not surprising since ELDORA only collected data on the cold front for ~ 1 min during each pass. Accordingly, the error in the time-space adjustment would be less than one grid point.

The aircraft motion was removed from the velocity data by using SOLO software (Oye et al. 1995). A Cressman filter (Cressman 1959) was applied in the interpolation process with a radius of influence of 600 and 300 m in the horizontal and vertical directions, respectively. The

synthesis of the radar data used CEDRIC (Custom Editing and Display of Reduced Information in Cartesian space; Mohr et al. 1986). The hydrometeor fall speeds were estimated from the reflectivity-terminal fall speed relationship established by Joss and Waldvogel (1970) with a correction for the effects of air density (Foote and du Toit 1969). A three-step Leise filter (Leise 1982) was applied to the Doppler wind syntheses which removes wavelengths of less than 4.8 km.

The vertical velocities were obtained from the anelastic continuity equation by upward integration of the horizontal convergence field. The estimated standard deviations for the derived vertical velocities were 1-2 ms^{-1} , although Wilson et al. (1994) suggest that these deviations may be even lower. The analyses presented in Fig. 7 were based on an average of 80 consecutive vertical cross sections. This averaging significantly reduces the standard deviations of vertical velocity, vertical vorticity and horizontal component of the wind shown in the figure.

References

- Asai, T., 1970: Three-dimensional features of thermal convection in a plane Couette flow. *J. Meteor. Soc. Japan*, **48**, 18-29.
- Atkins, N.T., R.M. Wakimoto, and C.L. Ziegler, 1998: Observations of the finescale structure of a dryline during VORTEX 95: *Mon. Wea. Rev.*, **126**, 525-550.
- Browell, E.V., S. Ismail, W.M. Hall, A.S. Moore, Jr., S.A. Kooi, V.G. Brackett, M.B. Clayton, J.D.W. Barrick, F.J. Schmidlin, N.S. Higdon, S.H. Melfi, and D.N. Whiteman, 1997: LASE validation experiment, in *Advances in Atmospheric Remote Sensing with Lidar*, A. Ansmann, R. Neuber, P. Rairoux, and U. Wandinger, eds., Springer-Verlag, Berlin, 289-295.
- _____, _____, R.A. Ferrare, S.A. Kooi, A. Notari, C.F. Butler, V.G. Brackett, H.E. Revercomb, P. Antonelli, 2003: Airborne remote measurements of water vapor, relative humidity, aerosol, and cloud distributions during the IHOP field experiment, *6th International Symposium on Tropospheric Profiling*, Leipzig, Germany, Institute for Tropospheric Research, 384-386.
- Bluestein, H.B., and C.R. Parks, 1983: A synoptic and photographic climatology of low-precipitation severe thunderstorms in the Southern Plains. *Mon. Wea. Rev.*, **111**, 2034-2046.
- _____, and S.S. Parker, 1993: Modes of isolated, severe convective storm formation along the dryline. *Mon. Wea. Rev.*, **121**, 1352-1374.
- _____, E.W. McCaul, G.P. Byrd, R.L. Walko, and R. Davies-Jones, 1990: An observational study of splitting convective clouds. *Mon. Wea. Rev.*, **118**, 1359-1370.
- Brown, R.A., 1980: Longitudinal instabilities and secondary flows in the planetary boundary

- layer: A review. *Rev. Geophys. Space Phys.*, **18**, 683-697.
- Crawford, T.M., and H.B. Bluestein, 1997: Characteristics of dryline passage during COPS-91. *Mon. Wea. Rev.*, **125**, 463-477.
- Cressman, G.P., 1959: An operational objective analysis scheme. *Mon. Wea. Rev.*, **87**, 367-384.
- Doswell, C.A., and L.F. Bosart, 2001: Extratropical synoptic-scale processes and severe convection. Severe Convective Storms. *Meteor. Monogr.*, No. 50, Amer. Meteor. Soc., 27-69.
- Doviak, R.J., and D.S. Zrnic, 1993: *Doppler radar and weather observations*. Academic Press, Inc., New York, 562 pp.
- Foot, G.B., and R.S. du Toit, 1969: Terminal velocity of raindrops aloft. *J. Appl. Meteor.*, **8**, 249-253.
- Hane, C.E., C.L. Ziegler, and H.B. Bluestein, 1993: Investigation of the dryline and convective storms initiated along the dryline: Field experiments during COPS-91. *Bull. Amer. Meteor. Soc.*, **74**, 2133-2145.
- _____, B.B. Bluestein, T.M. Crawford, M.E. Baldwin, and R.M. Rabin, 1997: Severe thunderstorm development in relation to along-dryline variability: A case study. *Mon. Wea. Rev.*, **125**, 231-251.
- _____, M.E. Baldwin, H.B. Bluestein, T.M. Crawford, and R.M. Rabin, 2001: A case study of severe storm development along a dryline within a synoptically active environment. Part I: Dryline motion and an eta model forecast. *Mon. Wea. Rev.*, **129**, 2183-2204.
- _____, R.M. Rabin, T.M. Crawford, H.B. Bluestein, and M.E. Baldwin, 2002: A case study

- of severe storm development along a dryline within a synoptically active environment: Part II: Multiple boundaries and convective initiation. *Mon. Wea. Rev.*, **130**, 900-920.
- Hildebrand, P.H., C.A. Walther, C.L. Frush, J. Testud, and F. Baudin, 1994: The ELDORA/ASTRAIA airborne Doppler weather radar: Goals, design, and first field tests. *Proceedings of the IEEE*, **82**, 1873-1890.
- _____, W.-C. Lee, C.A. Walther, C. Frush, M. Randall, E. Loew, R. Neitzel, R. Parsons, J. Testud, F. Baudin, A. LeCornec, 1996: The ELDORA/ASTRAIA airborne Doppler weather radar: High resolution observations from TOGA COARE. *Bull. Amer. Meteor. Soc.*, **76**, 213-232.
- Hobbs, P.V., and K.R. Biswas, 1979: The cellular structure of narrow cold-frontal rainbands. *Quart. J. Roy. Meteor. Soc.*, **105**, 723-727.
- James, P.K., and K.A. Browning, 1979: Mesoscale structure of line convection at surface cold fronts. *Quart. J. Roy. Meteor. Soc.*, **105**, 371-382.
- Jorgensen, D.P., T. Matejka, and J.D. DuGranrut, 1996: Multi-beam techniques for deriving wind fields from airborne Doppler radars. *J. Meteor. Atmos. Physics*, **59**, 83-104.
- Joss, J., and D. Waldvogel, 1970: Raindrop size distribution and Doppler velocities. Preprints, *14th Conf. on Radar Meteorology*, Tucson, AZ, Amer. Meteor. Soc., 153-156.
- Koch, S.E., and J. McCarthy, 1982: The evolution of an Oklahoma dryline: Part II: Boundary-layer forcing of mesoconvective systems. *J. Atmos. Sci.*, **39**, 237-257.
- Kuettner, J.P., 1959: The band structure of the atmosphere. *Tellus*, **2**, 267-294.

- LeMone, M.A., 1973: The structure and dynamics of horizontal roll vortices in the planetary boundary layer. *J. Atmos. Sci.*, **30**, 1077-1091.
- Leise, J.A., 1982: A multidimensional scale-telescoped filter and data extension package. NOAA Tech. Memo. ERL-82, 11 pp. [Available from NOAA ERL, 325 Broadway, Boulder, CO 80303.]
- Mohr, C.G., L.J. Miller, R.L. Vaughn, and H.W. Frank, 1986: The merger of mesoscale datasets into a common Cartesian format for efficient and systematic analysis. *J. Atmos. Oceanic Technol.*, **3**, 146-161.
- Neiman, P.J., and R.M. Wakimoto, 1999: The interaction of a Pacific cold front with shallow air masses east of the Rocky Mountains. *Mon. Wea. Rev.*, **127**, 2102-2127.
- Ogura, Y., H.-M. Juang, K.-S. Zhang, and S.-T. Soong, 1982: Possible triggering mechanisms for severe storms in SESAME-AVE IV (9-10 May 1979). *Bull. Amer. Meteor. Soc.*, **63**, 503-515.
- Oye, R., C. Mueller, and S. Smith, 1995: Software for radar translation, visualization, editing, and interpolation. Preprints, *27th Conf. on Radar Meteorology*, Vail, CO, Amer. Meteor. Soc., 359-361.
- Parsons, D.B., M.A. Shapiro, R.M. Hardesty, R.J. Zamora, and J.M. Intrieri, 1991: The finescale structure of a west Texas dryline. *Mon. Wea. Rev.*, **119**, 1242-1258.
- _____, _____, and E. Miller, 2000: The mesoscale structure of a nocturnal dryline and of a frontal-dryline merger. *Mon. Wea. Rev.*, **128**, 3824-3838.

Purdum, J.F.W., 1982: Subjective interpretations of geostationary satellite data for nowcasting.

Nowcasting, K. Browning, Ed., Academic Press, 149-166.

Reed, R.J., and M.D. Albright, 1997: Frontal structure in the interior of an intense mature ocean cyclone. *Wea. Forecasting*, **12**, 866-876.

Rhea, J.O., 1966: A study of thunderstorm formation along drylines. *J. Appl. Meteor.*, **5**, 58-63.

Schaefer, J.T., 1974: The lifecycle of the dryline. *J. Appl. Meteor.*, **13**, 444-449.

_____, 1986: The dryline. *Mesoscale Meteorology and Forecasting*, P.S. Ray, Ed., Amer. Meteor. Soc., 549-572.

Shapiro, M.A., T. Hampel, D. Rotzoll, and F. Mosher, 1985: The frontal hydraulic head: A micro- α scale (~1 km) triggering mechanism for mesoconvective weather systems. *Mon. Wea. Rev.*, **113**, 1166-1183.

Shaw, B.L., R.A. Pielke, and C.L. Ziegler, 1997: A three-dimensional numerical simulation of a Great Plains dryline. *Mon. Wea. Rev.*, **125**, 1489-1506.

Simpson, J.E., 1997: *Gravity currents in the environment and the laboratory*. Cambridge University Press, New York, 244 pp.

Wakimoto, R.M., W.-C. Lee, H.B. Bluestein, C.-H. Liu, and P.H. Hildebrand, 1996: ELDORA observations during VORTEX 95. *Bull. Amer. Meteor. Soc.*, **77**, 1465-1481.

Weckwerth, T.M., J.W. Wilson, R.M. Wakimoto, and N.A. Crook, 1997: Horizontal convective rolls: Determining the environmental conditions supporting their existence and characteristics. *Mon. Wea. Rev.*, **125**, 505-526.

- _____, D.B. Parsons, S.E. Koch, J.A. Moore, M.A. LeMone, B.B. Demoz, C. Flamant, B. Geerts, J. Wang, and W.F. Feltz, 2004: An overview of the International H₂O Project (IHOP 2002) and some preliminary highlights. *Bull. Amer. Meteor. Soc.*, **85**, 253-277.
- Weiss, C.C., and H.B. Bluestein, 2002: Airborne pseudo-dual Doppler analysis of a dryline-outflow boundary intersection. *Mon. Wea. Rev.*, **130**, 1207-1226.
- Wilson, J.W., and W.E. Schreiber, 1986: Initiation of convective storms at radar-observed boundary-layer convergence lines. *Mon. Wea. Rev.*, **114**, 2516-2536.
- _____, T.M. Weckwerth, J. Vivekanandan, R.M. Wakimoto, and R.W. Russell, 1994: Boundary layer clear-air radar echoes: Origin of echoes and accuracy of derived winds. *J. Atmos. Oceanic Technol.*, **11**, 1184-1206.
- Young, G.S., and R.H. Johnson, 1984: Meso- and microscale features of a Colorado cold front. *J. Appl. Meteor.*, **23**, 1315-1325.
- Ziegler, C.L., and C.E. Hane, 1993: An observational study of the dryline. *Mon. Wea. Rev.*, **121**, 1134-1151.
- _____, and E.N. Rasmussen, 1998: The initiation of moist convection at the dryline: Forecasting issues from a case study perspective. *Wea. Forecasting*, **13**, 1106-1131.
- _____, W.J. Martin, R.A. Pielke, and R.L. Walko, 1995: A modeling study of the dryline. *J. Atmos. Sci.*, **52**, 273-285.

List of Tables

Table 1 ELDORA Scanning Mode

TABLE 1**ELDORA Scanning Mode**

Antenna rotation rate ($^{\circ} \text{ s}^{-1}$)	75
Number of samples	60
PRF (Hz)	3000
Gate length (m)	110
Sweep-angle resolution ($^{\circ}$)	1.5
Along-track resolution (m)	~ 550
Maximum range (km)	50
Maximum unambiguous velocities ($\pm \text{m s}^{-1}$)	23.6

Figure Captions

Fig. 1. Surface analyses superimposed onto visible satellite images at a) 1900 UTC, b) 2000 UTC, c) 2100 UTC, and 2200 UTC on 24 May 2002. The solid line in a), b) and c) and the dashed line in b) are the tracks of the P-3 and DC-8, respectively. Temperature and dew-point temperature are shown. Winds are plotted with the full barb and half barb representing 5 m s^{-1} and 2.5 m s^{-1} , respectively. The "X" in b) denotes the location of the eastern aerosol plum shown in Fig. 16.

Fig. 2. Surface analyses superimposed onto radar scans recorded by the WSR-88D located at Amarillo, TX at a) 1900 UTC, b) 2000 UTC, c) 2100 UTC, and d) 2200 UTC on 24 May 2002. The cold front and dryline symbols are not drawn continuously to the triple point on the figure so that it does not obscure the thin lines observed by the WSR-88D. The dotted line is the track of the NRL P-3. Dash-dot line in b) is the track of the DC-8. Open circles in b) represent the locations of dropsondes. The "X" in b) denotes the location of the eastern aerosol plume shown in Fig. 16. The solid and dashed boxes represent dual-Doppler analysis regions shown in Figs. 3, 8, 9, 12, and 15. The analysis times are shown in the bottom right corner in a), b), and c). Temperature and dew-point temperature are plotted. Winds are plotted with the full barb and half barb representing 5 m s^{-1} and 2.5 m s^{-1} , respectively.

Fig. 3. Dual-Doppler wind synthesis at 1915:01 - 1926:52 UTC at 600 m AGL. a) Radar reflectivity. b) Vertical velocity and vertical vorticity. The short black line represents the location of the

raw ELDORA scan shown in Fig. 6. The dashed black line represents the track of the P-3. Flight-level winds at ~450 m AGL are plotted along the track. Winds are plotted with the full barb and half barb representing 5 m s^{-1} and 2.5 m s^{-1} , respectively. Positive and negative vertical velocities are drawn as gray and dashed-gray lines, respectively. Positive and negative vertical vorticity are drawn as black and dashed lines, respectively. Radar reflectivities greater than 4 dBZe in b) are shaded gray. Black box is enlarged in Fig. 4.

Fig. 4. Dual-Doppler wind synthesis, vertical vorticity, vertical velocity, and radar reflectivity at a) 1915:01 - 1926:52 UTC, b) 1931:32 - 1942:45 UTC, c) 1949:35 - 1959:54 UTC, and d) 2004:04 - 2014:30 UTC. Black and short dashed lines represent positive and negative vertical vorticity. Long dashed and dashed-dot lines represent positive and negative vertical velocity, respectively. Flight tracks of the P-3 and DC-8 are shown. Flight-level winds are plotted along the P-3 track. Winds are plotted with the full barb and half barb representing 5 m s^{-1} and 2.5 m s^{-1} , respectively. Cross sections labeled AA' and BB' are shown in Fig. 11.

Fig. 5. Flight-level data from the NRL P-3 as it penetrated the cold front and dryline at 400 m AGL. Equivalent and virtual potential temperature, wind direction and speed, and mixing ratio are plotted. a) 1922:12 - 1926:24 UTC. b) 1910:48 - 1913:12 UTC. Time increases from right to left in b).

Fig. 6. Range-Height Indicator (RHI) cross section of radar reflectivity and single-Doppler velocity through the dryline at 1917:53 UTC. Approximate flow pattern shown in the figure based on single-Doppler velocities. The locations of the scan is shown in Fig. 3.

Fig. 7. Mean vertical cross section of the dryline for 1915:01 - 1926:40 UTC. Radar reflectivity superimposed onto a) vertical velocity, b) vertical vorticity, and c) the u' -component of the wind in the rotated domain. Reflectivities greater than 6 dBZe are shaded gray. The mean vectors plotted in a) and c) are the component of flow in the plane of the cross section. Mean winds are plotted in b).

Fig. 8. Same as Fig. 3, except the period 1931:32 - 1942:45 UTC at 600 m AGL.

Fig. 9. Same as Fig. 3, except the period 1949:35 - 1959:54 UTC at 600 m AGL. The short black lines represent the location of the raw ELDORA scans shown in Fig. 10.

Fig. 10. Sequence of RHI images of radar reflectivity and single-Doppler velocity of the merger between the cold front and the dryline at a) 1957:10 UTC, b) 1957:32 UTC, and c) 1957:53 UTC. Approximate flow patterns are shown by the curved black arrows and are based on single-Doppler velocities. The short black arrows in b) indicate the position of three rotational couplets.

Fig. 11. Vertical cross sections along lines AA' and BB' depicted in Fig. 4c. Radar reflectivity and dual-Doppler winds in the plane of the cross section are plotted on the top panels. Radar reflectivity and the total horizontal wind are plotted on the bottom panels. Radar reflectivities greater than 6 dBZe are shaded gray.

Fig. 12. Same as Fig. 3, except the period 2004:04 - 2014:30 UTC at 600 m AGL. Dashed box is enlarged in Fig. 13.

Fig. 13. Dual-Doppler wind synthesis at 2004:04 - 2014:30 UTC at 600 m AGL focused on the double-fine line structure. a) Radar reflectivity, b) isogons of the wind field. Flight-level winds are plotted along the track. Winds are plotted with the full barb and half barb representing 5 m s⁻¹ and 2.5 m s⁻¹, respectively. Radar reflectivities greater than 4 dBZe in b) are shaded gray.

Fig. 14. Flight-level data from the NRL P-3 as it penetrated the cold front and the double-fine line at 400 m AGL for 2006 - 2012 UTC. Equivalent and virtual potential temperature, wind direction and speed, and mixing ratio are plotted.

Fig. 15. Dual-Doppler wind syntheses superimposed onto radar reflectivity at a) 2024:01 - 2034:31 and b) 2038:51 - 2049:28 UTC at 600 m AGL. Short dashed line represents the track of the P-3. Flight level winds are plotted along the track. Winds are plotted with the full barb and half barb

representing 5 m s^{-1} and 2.5 m s^{-1} , respectively.

Fig. 16. Vertical cross sections based on the lidar (color shading) and dropsonde data (solid contours and winds). a) Mixing ratio analysis and wind profiles from the dropsonde data superimposed onto the retrieved mixing ratio derived from lidar data. b) Virtual potential temperature and wind profiles from dropsonde data superimposed onto the aerosol scattering ratio derived from lidar data. c) Equivalent potential temperature and wind profiles from the dropsonde data superimposed onto the aerosol scattering ratio derived from lidar data. The lidar data were recorded by the LASE onboard the DC-8. The flight times of the DC-8 are shown at the top of the figure. Winds are plotted with the full barb and half barb representing 5 m s^{-1} and 2.5 m s^{-1} , respectively. The position of the triple point is indicated at the bottom of the figure. The thick dashed line represents the location of the ground. Heights are above mean sea level (MSL). The location of the aerosol plume to the east of the triple point is shown in Figs. 1b and 2b.

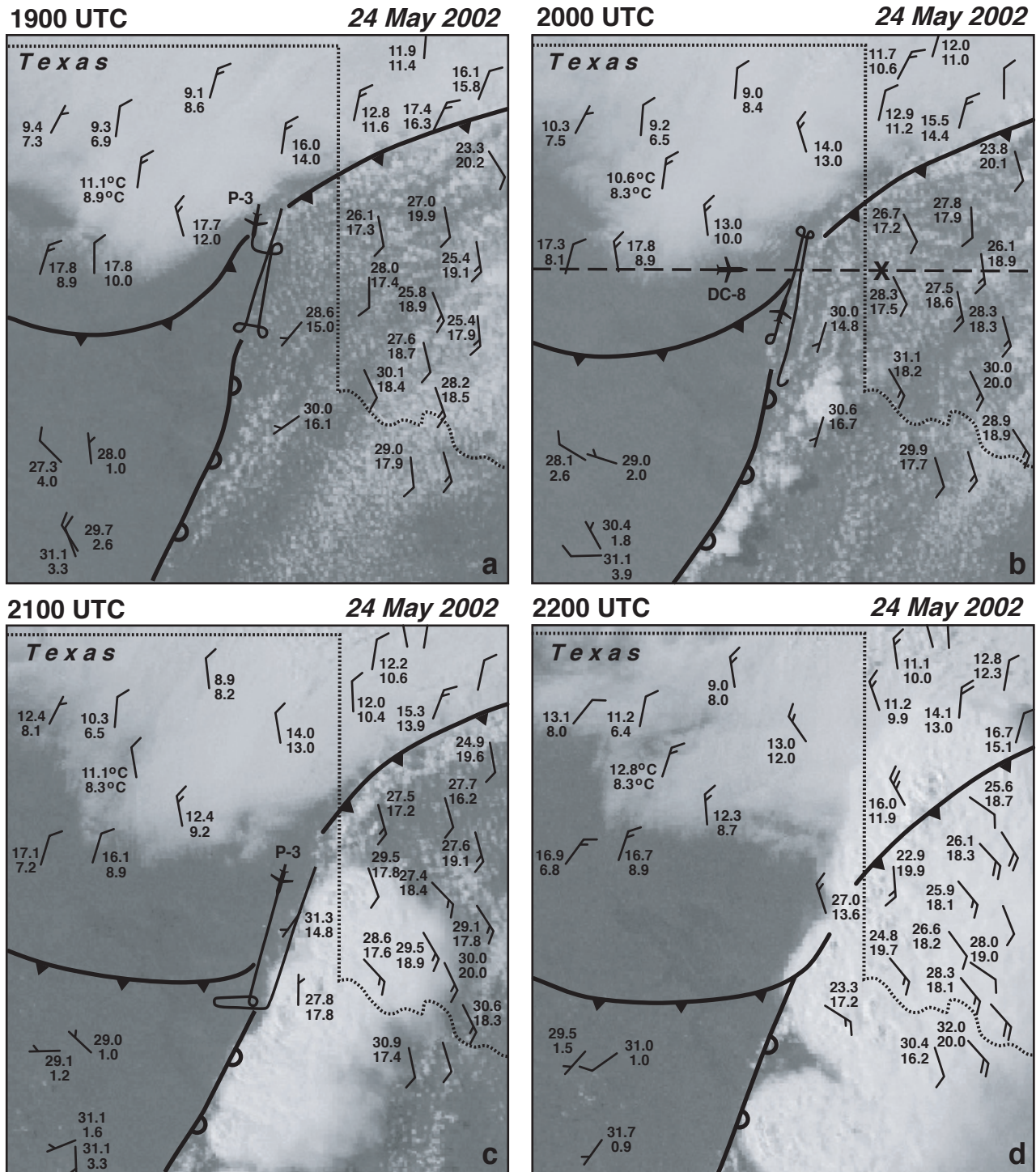


Fig. 1. Surface analyses superimposed onto visible satellite images at a) 1900 UTC, b) 2000 UTC, c) 2100 UTC, and d) 2200 UTC on 24 May 2002. The solid line in a), b) and c) and the dashed line in b) are the tracks of the P-3 and DC-8, respectively. Temperature and dew-point temperature are shown. Winds are plotted with the full barb and half barb representing 5 m s⁻¹ and 2.5 m s⁻¹, respectively. The "X" in b) denotes the location of the eastern aerosol plume shown in Fig. 16.

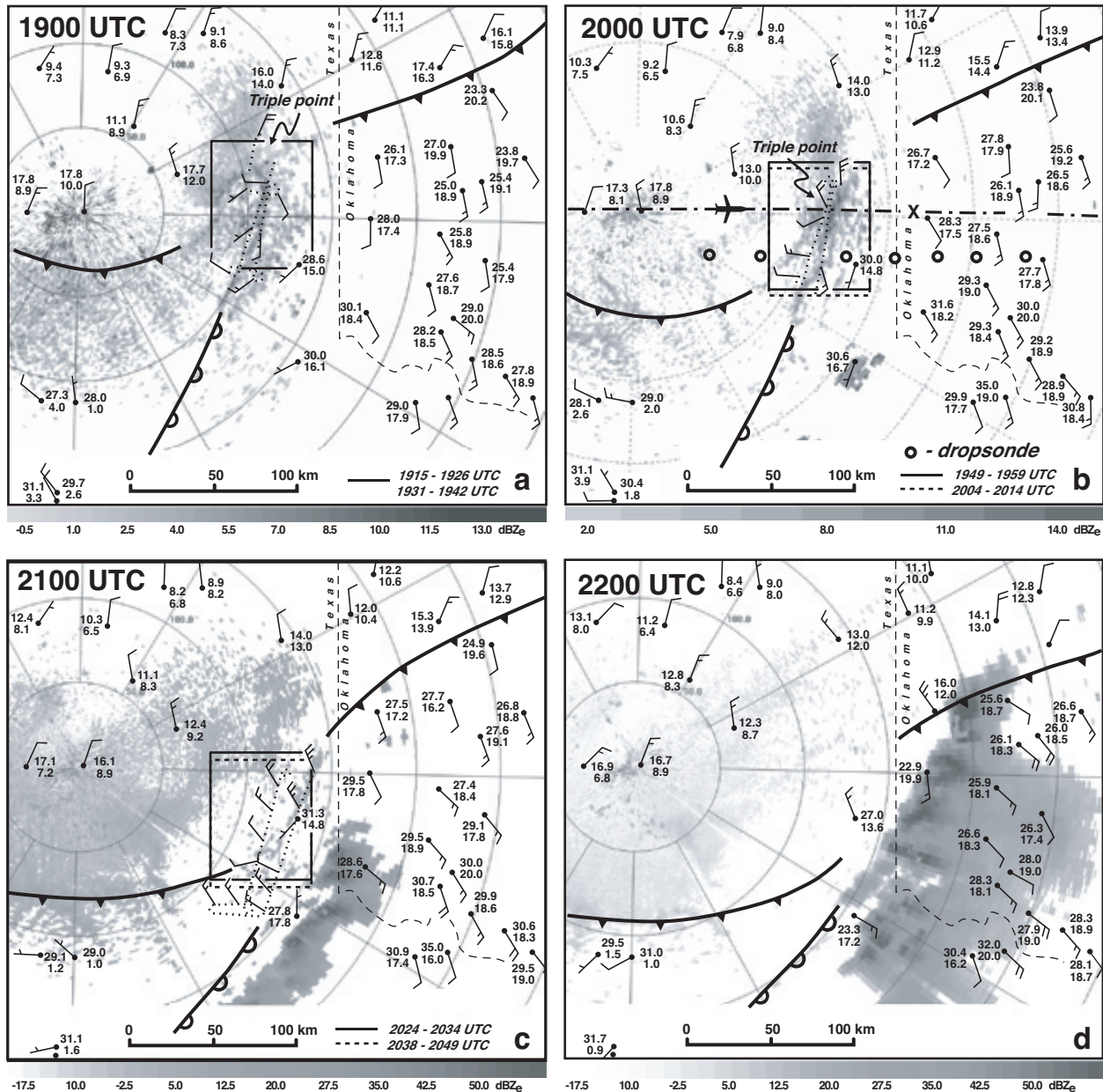


Fig. 2. Surface analyses superimposed onto radar scans recorded by the WSR-88D located at Amarillo, TX at a) 1900 UTC, b) 2000 UTC, c) 2100 UTC, and d) 2200 UTC on 24 May 2002. The cold front and dryline symbols are not drawn continuously to the triple point on the figure so that it does not obscure the thin lines observed by the WSR-88D. The dotted line is the track of the NRL P-3. Dash-dot line in b) is the track of the DC-8. Open circles in b) represent the locations of dropsondes. The "X" in b) denotes the location of the eastern aerosol plume shown in Fig. 16. The solid and dashed boxes represent dual-Doppler analysis regions shown in Figs. 3, 8, 9, 12, and 15. The analysis times are shown in the bottom right corner in a), b), and c). Temperature and dew-point temperature are plotted. Winds are plotted with the full barb and half barb representing 5 m s⁻¹ and 2.5 m s⁻¹, respectively.

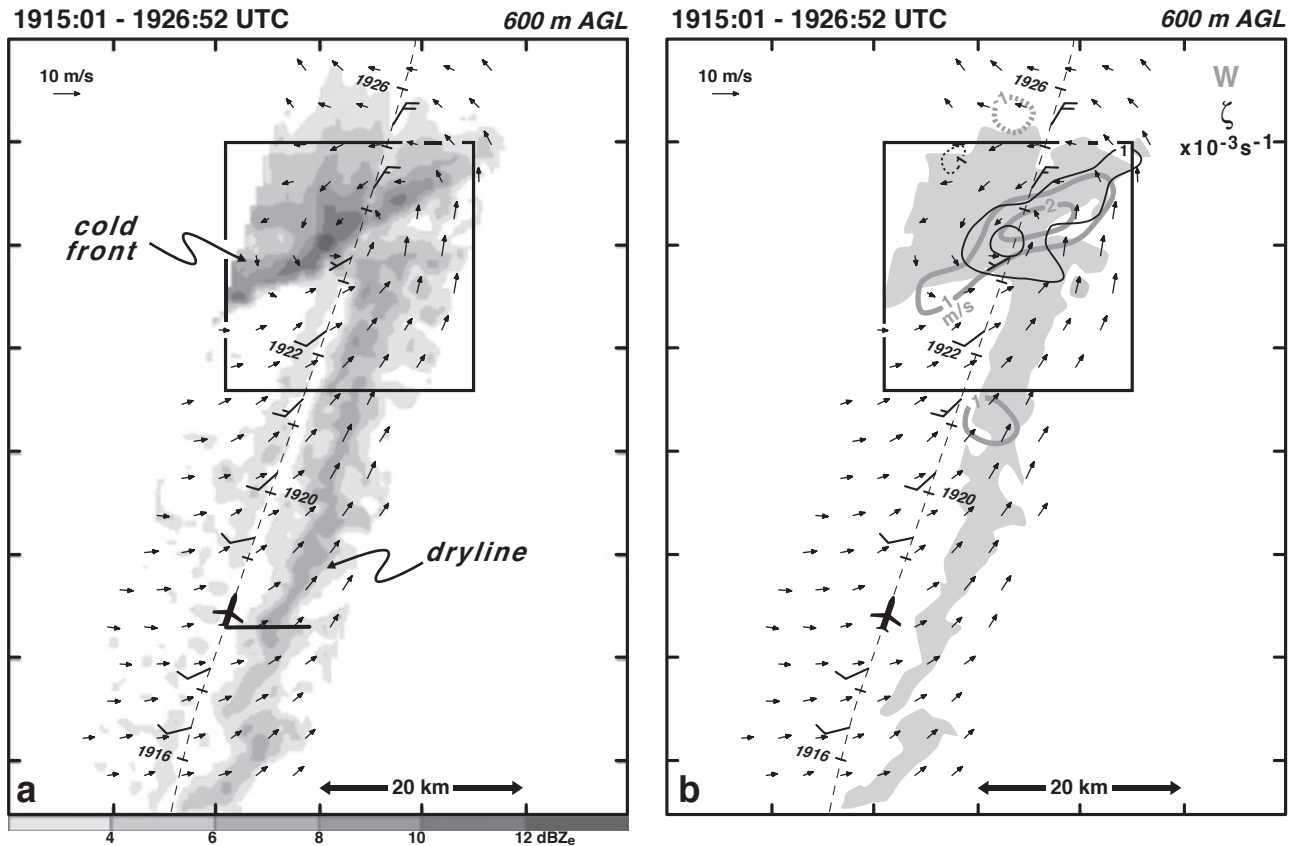


Fig. 3. Dual-Doppler wind synthesis at 1915:01 - 1926:52 UTC at 600 m AGL. a) Radar reflectivity. b) Vertical velocity and vertical vorticity. The short black line represents the location of the raw ELDORA scan shown in Fig. 6. The dashed black line represents the track of the P-3. Flight-level winds at ~ 450 m AGL are plotted along the track. Winds are plotted with the full barb and half barb representing 5 m s^{-1} and 2.5 m s^{-1} , respectively. Positive and negative vertical velocities are drawn as gray and dashed-gray lines, respectively. Positive and negative vertical vorticity are drawn as black and dashed lines, respectively. Radar reflectivities greater than 4 dBZe in b) are shaded gray. Black box is enlarged in Fig. 4.

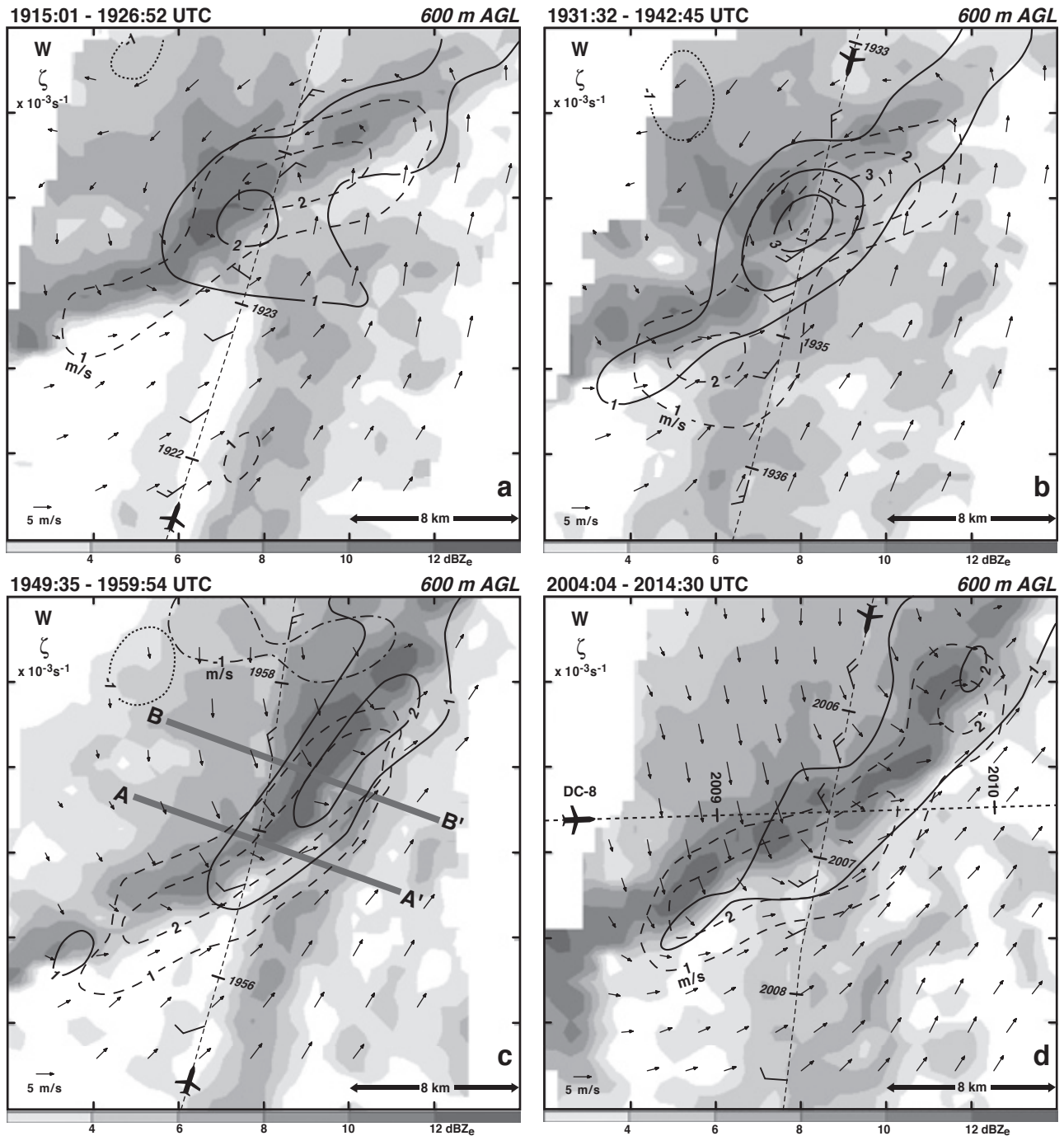


Fig. 4. Dual-Doppler wind synthesis, vertical vorticity, vertical velocity, and radar reflectivity at a) 1915:01 - 1926:52 UTC, b) 1931:32 - 1942:45 UTC, c) 1949:35 - 1959:54 UTC, and d) 2004:04 - 2014:30 UTC. Black and short dashed lines represent positive and negative vertical vorticity. Long dashed and dashed-dot lines represent positive and negative vertical velocity, respectively. Flight tracks of the P-3 and DC-8 are shown. Flight-level winds are plotted along the P-3 track. Winds are plotted with the full barb and half barb representing 5 m s^{-1} and 2.5 m s^{-1} , respectively. Cross sections labeled AA' and BB' are shown in Fig. 11.

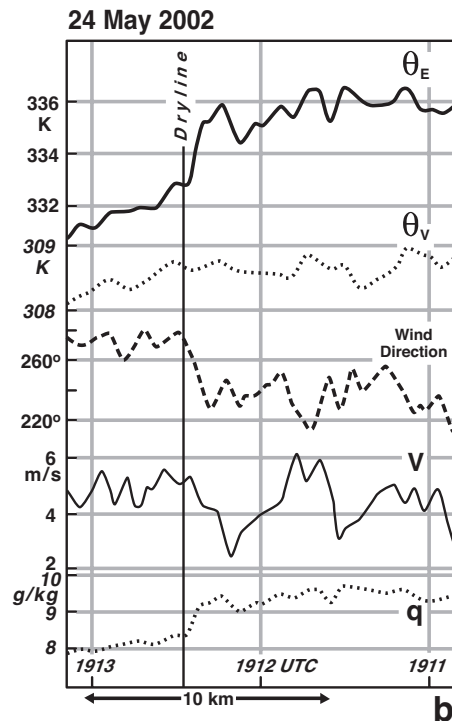
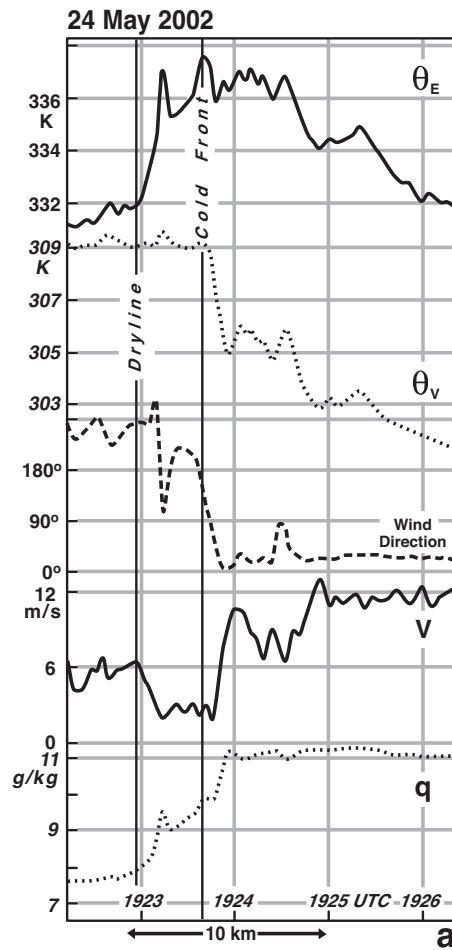


Fig. 5. Flight-level data from the NRL P-3 as it penetrated the cold front and dryline at 400 m AGL. Equivalent and virtual potential temperature, wind direction and speed, and mixing ratio are plotted. a) 1922:12 - 1926:24 UTC. b) 1910:48 - 1913:12 UTC. Time increases from right to left in b).

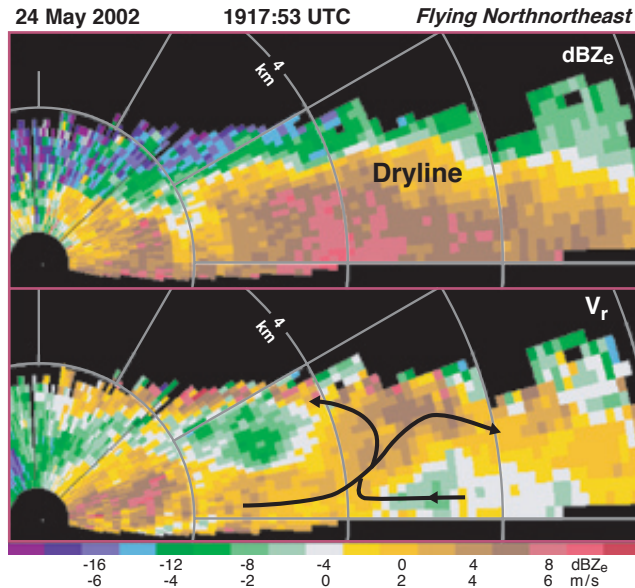


Fig. 6. Range-Height Indicator (RHI) cross section of radar reflectivity and single-Doppler velocity through the dryline at 1917:53 UTC. Approximate flow pattern shown in the figure based on single-Doppler velocities. The locations of the scan is shown in Fig. 3.

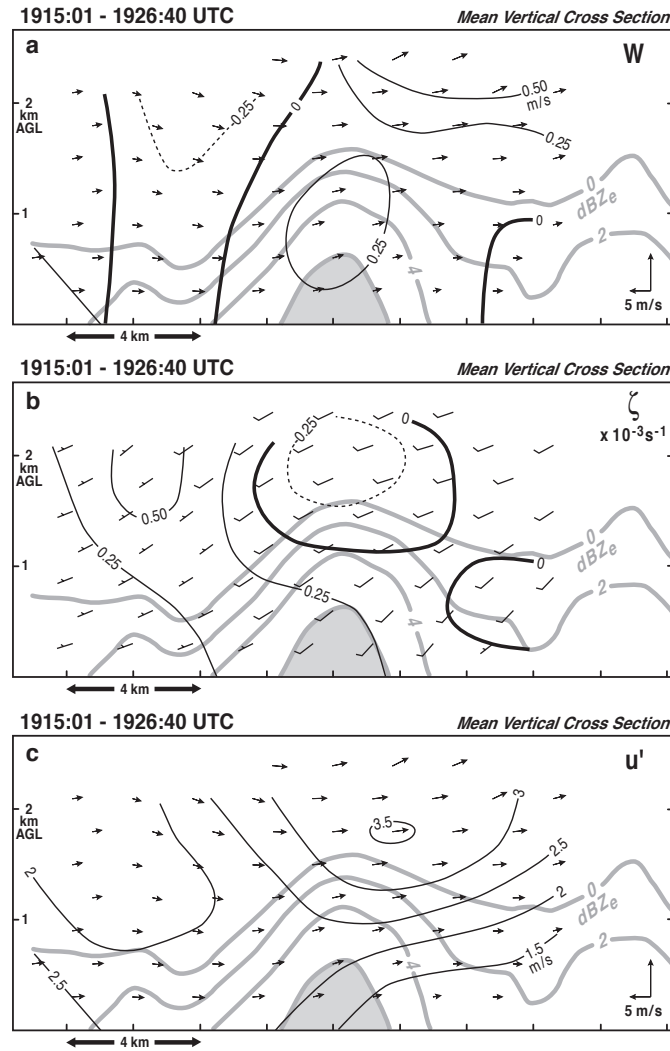


Fig. 7. Mean vertical cross section of the dryline for 1915:01 - 1926:40 UTC. Radar reflectivity superimposed onto a) vertical velocity, b) vertical vorticity, and c) the u' -component of the wind in the rotated domain. Reflectivities greater than 6 dBZe are shaded gray. The mean vectors plotted in a) and c) are the component of flow in the plane of the cross section. Mean winds are plotted in b).

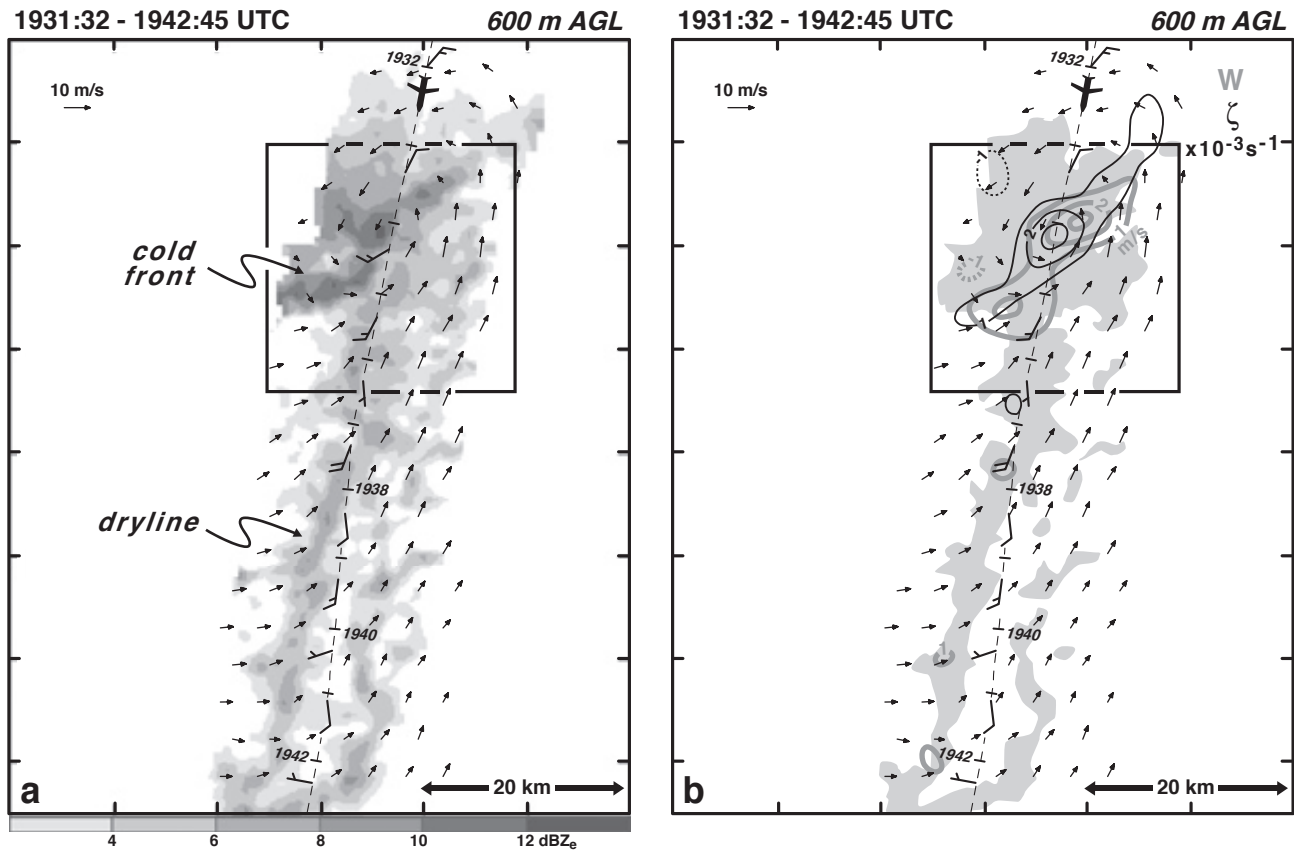


Fig. 8. Same as Fig. 3, except the period 1931:32 - 1942:45 UTC at 600 m AGL.

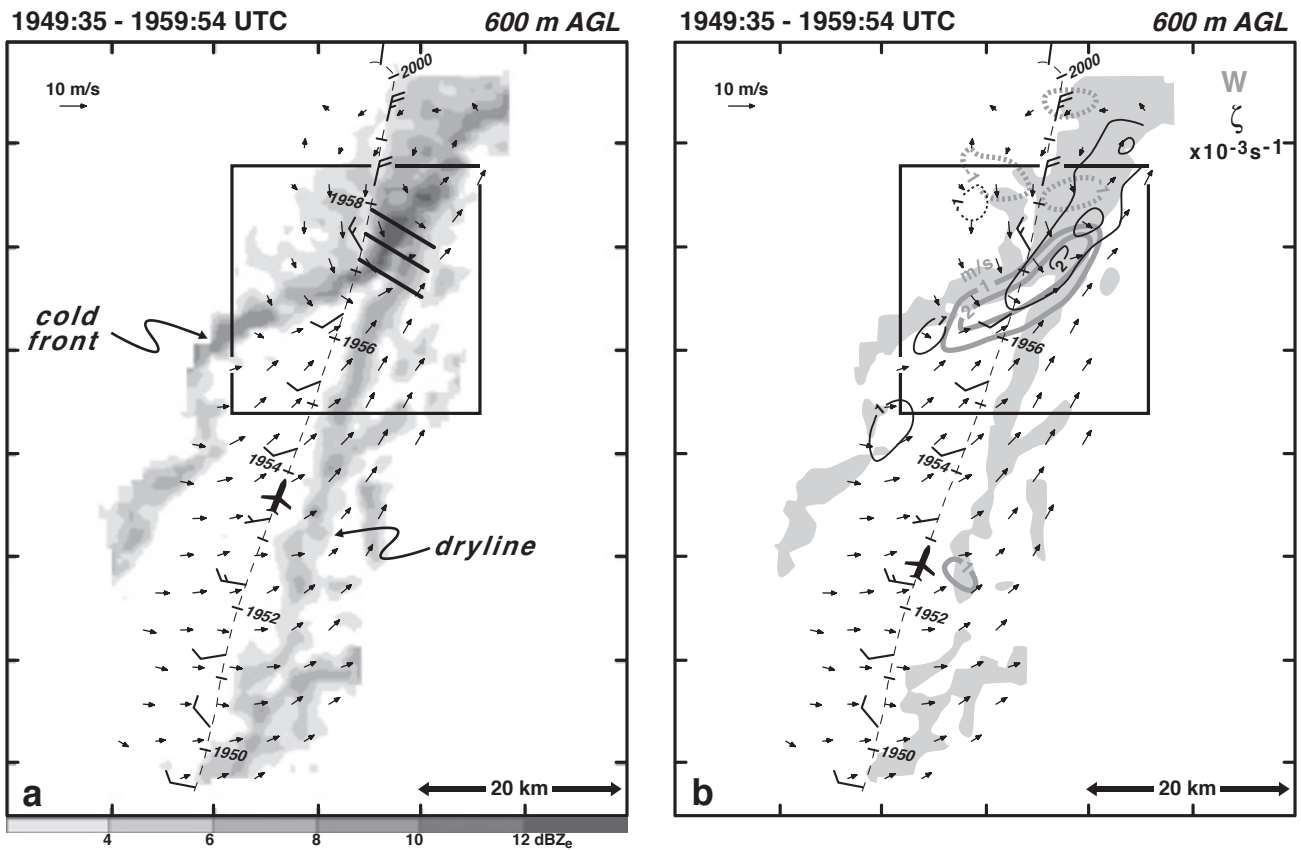


Fig. 9. Same as Fig. 3, except the period 1949:35 - 1959:54 UTC at 600 m AGL. The short black lines represent the location of the raw ELDORA scans shown in Fig. 10.

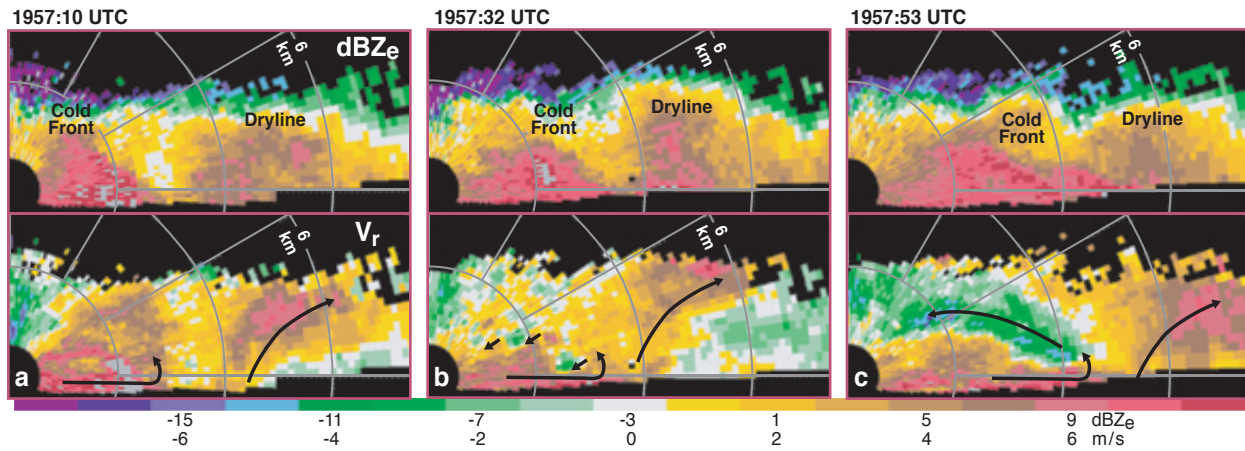


Fig. 10. Sequence of RHI images of radar reflectivity and single-Doppler velocity of the merger between the cold front and the dryline at a) 1957:10 UTC, b) 1957:32 UTC, and c) 1957:53 UTC. Approximate flow patterns are shown by the curved black arrows and are based on single-Doppler velocities. The short black arrows in b) indicate the position of three rotational couplets.

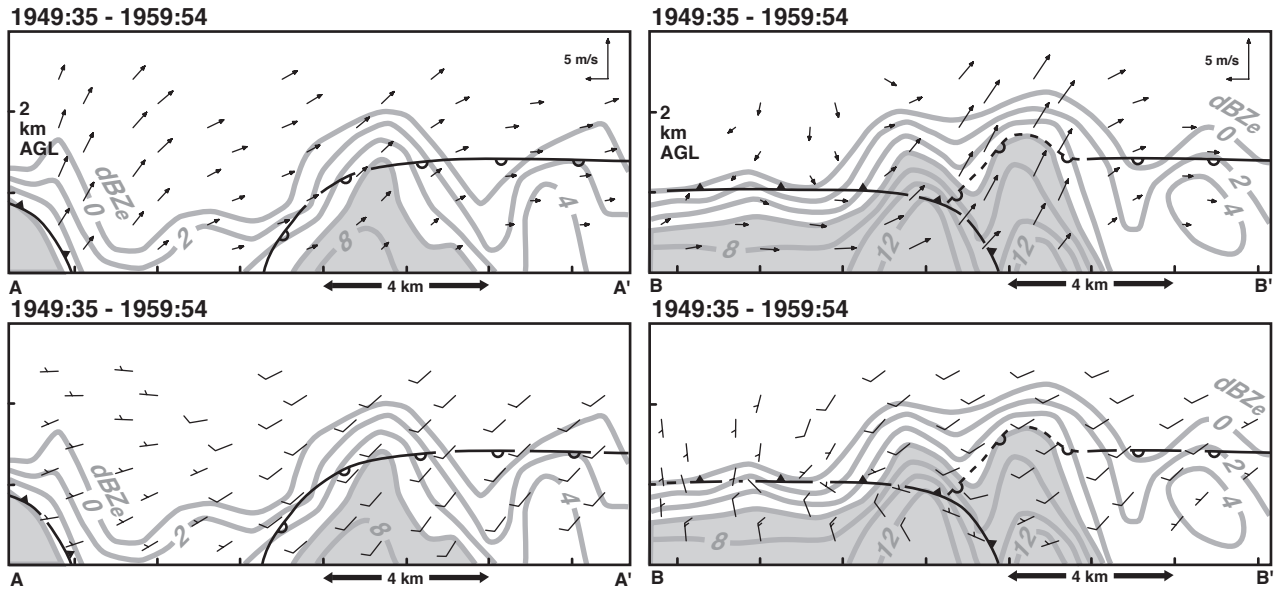


Fig. 11. Vertical cross sections along lines AA' and BB' depicted in Fig. 4c. Radar reflectivity and dual-Doppler winds in the plane of the cross section are plotted on the top panels. Radar reflectivity and the total horizontal wind are plotted on the bottom panels. Radar reflectivities greater than 6 dBZe are shaded gray.

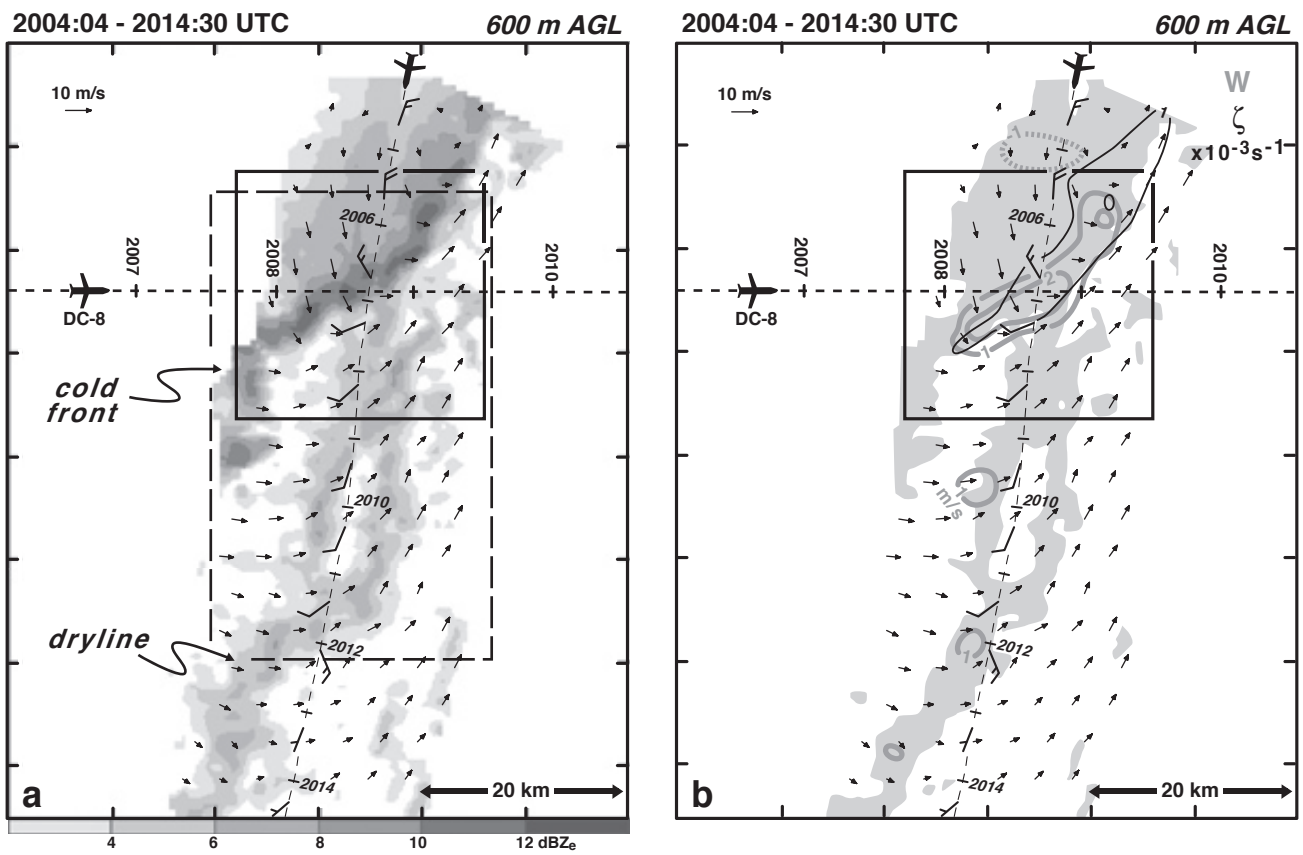


Fig. 12. Same as Fig. 3, except the period 2004:04 - 2014:30 UTC at 600 m AGL. Dashed box is enlarged in Fig. 13.

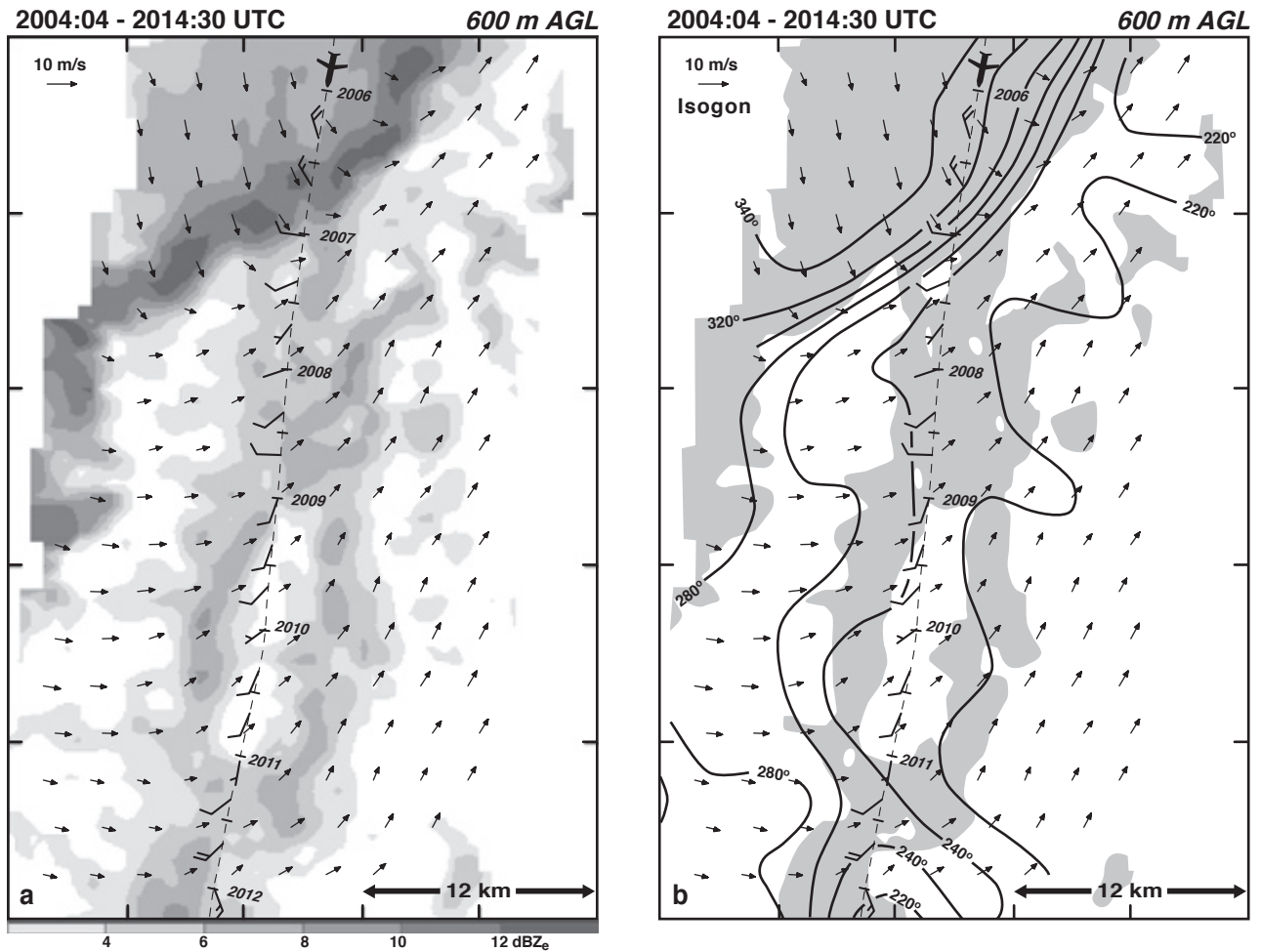


Fig. 13. Dual-Doppler wind synthesis at 2004:04 - 2014:30 UTC at 600 m AGL focused on the double-fine line structure. a) Radar reflectivity, b) isogons of the wind field. Flight-level winds are plotted along the track. Winds are plotted with the full barb and half barb representing 5 m s⁻¹ and 2.5 m s⁻¹, respectively. Radar reflectivities greater than 4 dBZe in b) are shaded gray.

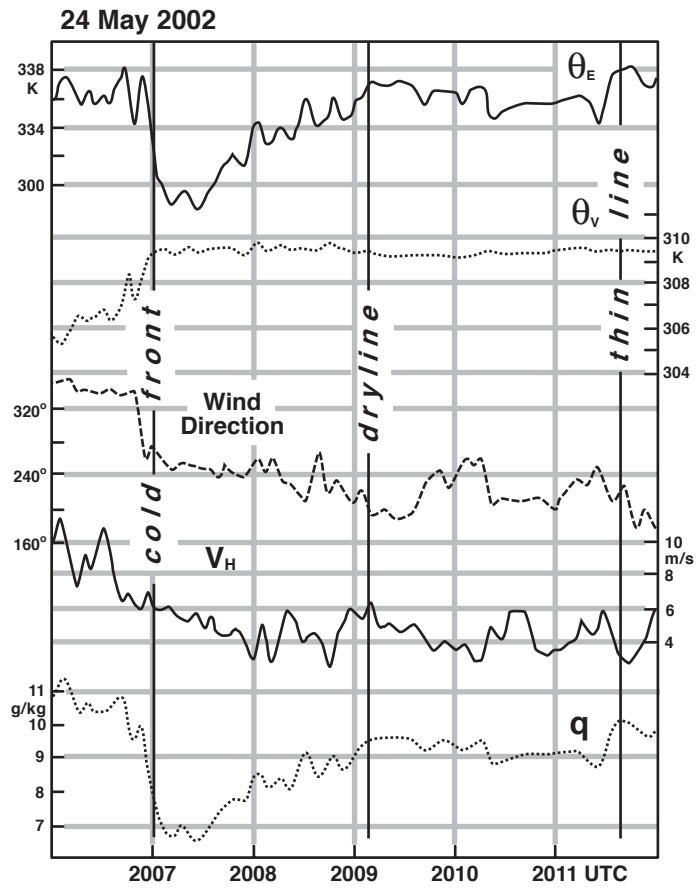


Fig. 14. Flight-level data from the NRL P-3 as it penetrated the cold front and the double-fine line at 400 m AGL for 2006 - 2012 UTC. Equivalent and virtual potential temperature, wind direction and speed, and mixing ratio are plotted.

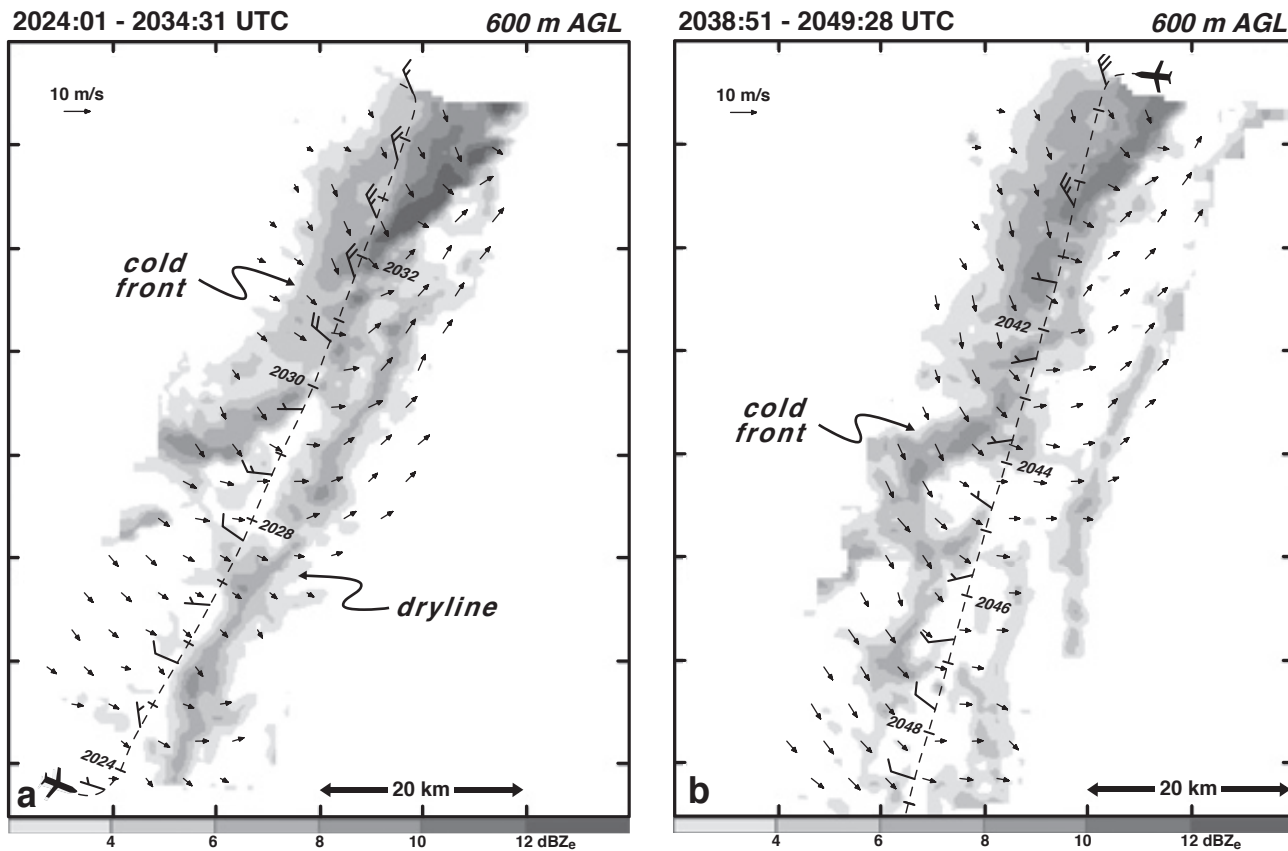
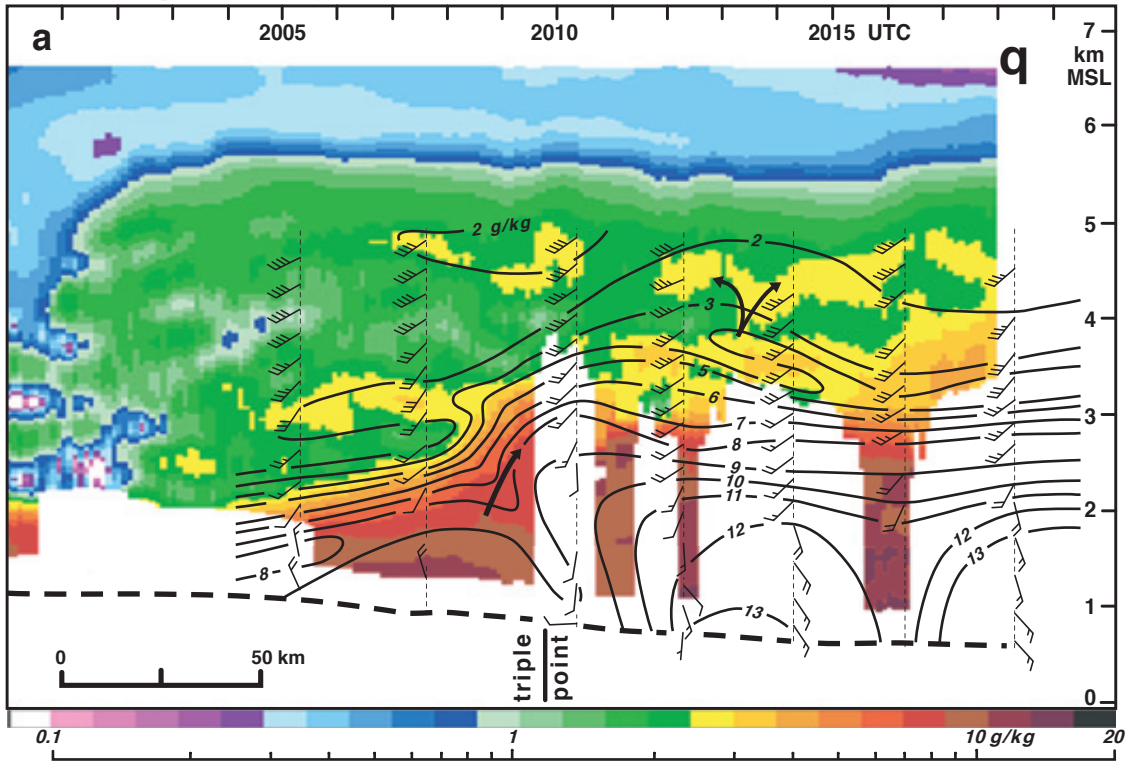
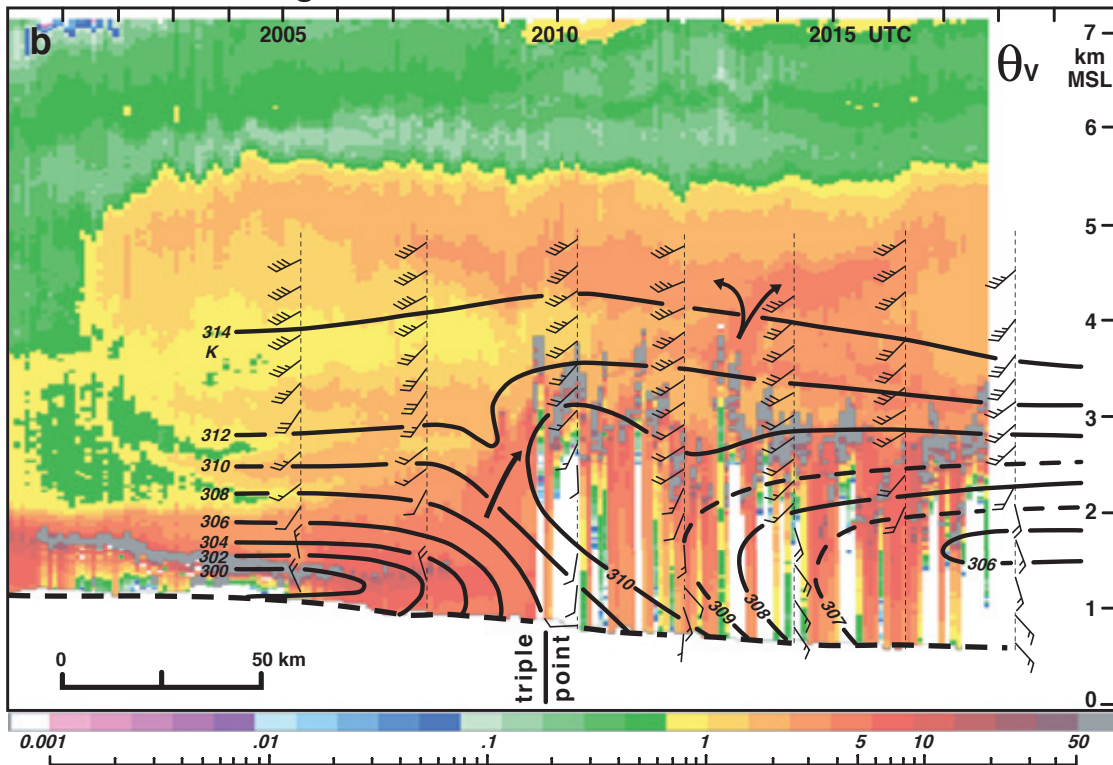


Fig. 15. Dual-Doppler wind syntheses superimposed onto radar reflectivity at a) 2024:01 - 2034:31 and b) 2038:51 - 2049:28 UTC at 600 m AGL. Short dashed line represents the track of the P-3. Flight level winds are plotted along the track. Winds are plotted with the full barb and half barb representing 5 m s^{-1} and 2.5 m s^{-1} , respectively.

Water Vapor Mixing Ratio



Aerosol Scattering Ratio



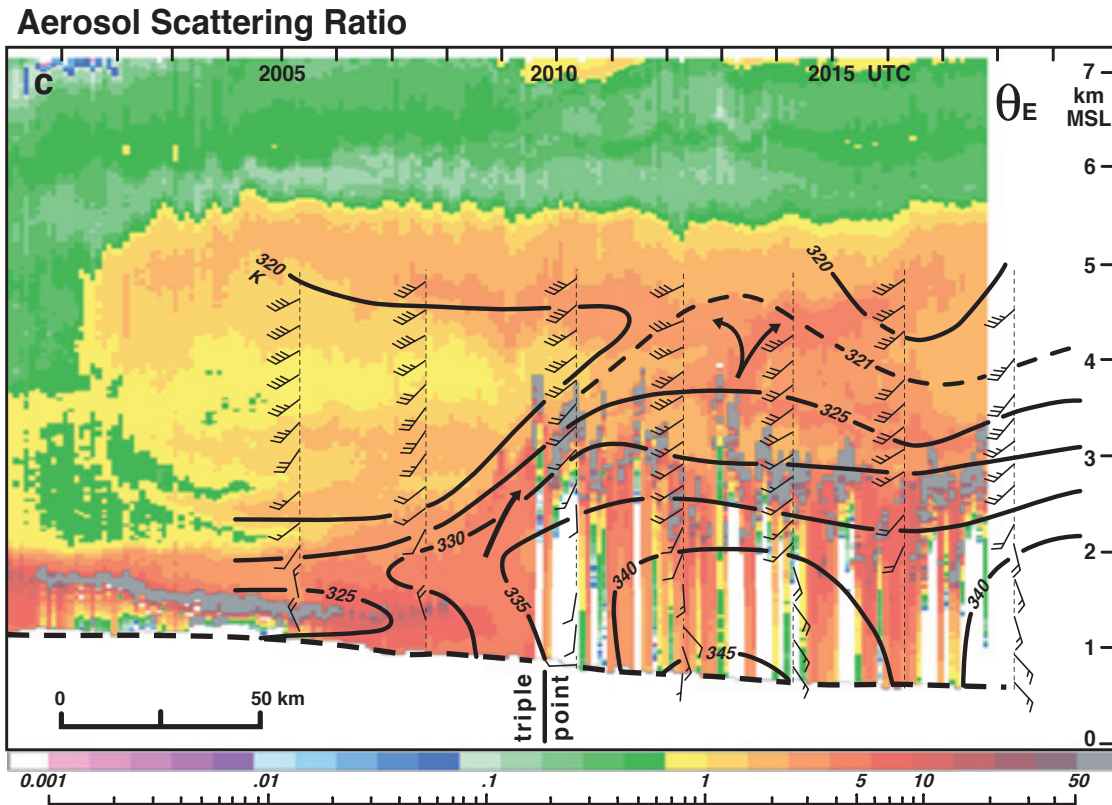


Fig. 16. Vertical cross sections based on the lidar (color shading) and dropsonde data (solid contours and winds). a) Mixing ratio analysis and wind profiles from the dropsonde data superimposed onto the retrieved mixing ratio derived from lidar data. b) Virtual potential temperature and wind profiles from dropsonde data superimposed onto the aerosol scattering ratio derived from lidar data. c) Equivalent potential temperature and wind profiles from the dropsonde data superimposed onto the aerosol scattering ratio derived from lidar data. The lidar data were recorded by the LASE onboard the DC-8. The flight times of the DC-8 are shown at the top of the figure. Winds are plotted with the full barb and half barb representing 5 m s^{-1} and 2.5 m s^{-1} , respectively. The position of the triple point is indicated at the bottom of the figure. The thick dashed line represents the location of the ground. Heights are above mean sea level (MSL). The location of the aerosol plume to the east of the triple point is shown in Figs. 1b and 2b.